Precambrian Research 255 (2014) 603–626

Contents lists available at ScienceDirect

Precambrian Research

journal homepage: www.elsevier.com/locate/precamres

Petrology and geochemistry of the Wangjiazhuang banded iron formation and associated supracrustal rocks from the Wutai greenstone belt in the North China Craton: Implications for their origin and tectonic setting

Changle Wang[a,b], Lianchang Zhang[a,*], Caiyun Lan[b,c], Yanpei Dai[a,b]

[a] Key Laboratory of Mineral Resources, Institute of Geology and Geophysics, Chinese Academy of Sciences, Beijing 100029, China
[b] University of Chinese Academy of Sciences, Beijing 100049, China
[c] Guangzhou Institute of Geochemistry, Chinese Academy of Sciences, Guangdong, Guangzhou 510640, China

ARTICLE INFO

Article history:
Received 21 July 2013
Received in revised form 21 July 2014
Accepted 2 August 2014
Available online 12 August 2014

Keywords:
Wutai greenstone belt
Algoma-type BIF
Tectonic setting of the BIF
Neoarchean
North China Craton (NCC)

ABSTRACT

The Wutai greenstone belt (WGB) is one of the most extensively studied greenstone belts in China. Together with the Hengshan and Fuping complexes, these three associations compose the central segment of the Trans-North China Orogen (TNCO) in the North China Craton (NCC). The Wangjiazhuang banded iron formation (BIF) is located in the bottom of the Jingangku Formation of the WGB. The associated supracrustal rocks consist of meta-basalts (amphibolites), meta-felsic volcanic rocks (leptynite) and metapelites (mica schist), which have experienced amphibolite-facies metamorphism. Amphibolites are commonly intercalated with the BIF. SIMS zircon U–Pb analyses on amphibolites suggest that the Wangjiazhuang BIF was formed at ca. 2543 ± 4 Ma. Combined with most Neoarchean Algoma-type BIFs in the NCC, these features indicate that a significant tectothermal event of the NCC have occurred at ~2.5 Ga. Mineral assemblages of the Wangjiazhuang BIF are composed of quartz, magnetite, amphibole, and minor garnet, pyrite and calcite. The precursor deposits of this BIF were likely ferric-oxyhydroxides, fine-grained carbonate oozes, silicate phases rich in Al–Ca–Mg–Fe and amorphous silica. The appearance of garnet and ferro-pargasite, high concentrations of Al_2O_3, HFSEs, Sc, and positive correlations among Al_2O_3, TiO_2, HFSEs and REE indicate that there was a significant terrigenous input. Even so, the Wangjiazhuang BIF samples display distinctively seawater-like REE+Y profiles, characterized by positive La and Y anomalies and HREE enrichment relative to LREE in PAAS-normalized REE diagrams. Consistently positive Eu anomalies are also observed, which are typically from high-T hydrothermal fluids. In addition, the true negative Ce anomalies recorded in the Wangjiazhuang BIF might indicate the onset of bottom-water oxidation at the Archean-Proterozoic boundary, at least in restricted basins. Amphibolites have geochemical affinity with both MORB- and arc-like components, and the trace element characteristics of leptynites are also consistent with a subduction zone signature. These features suggest that the Wangjiazhuang BIF was deposited in a back-arc basin. Oceanic subduction, coupled with contemporary depleted mantle upwelling related to back-arc basin extension, can account for the typical interaction between these two components.

1. Introduction

Banded iron formations (BIFs) are chemical sedimentary rocks (TFe > 15%) comprising alternating layers of iron-rich and silica-rich minerals that precipitated throughout Archean and early Paleoproterozoic (James, 1954; Trendall, 2002; Bekker et al., 2010). The mineral compositions of BIFs have been modified by diagenetic and metamorphic overprinting, and therefore, the main minerals now present in BIFs (e.g., quartz, hematite, magnetite, carbonates and ferrous silicates) are actually of secondary origin. The identity of the original sediments and relevant precipitation mechanism is a subject of debate. BIFs must have been derived from a precursor sediment that was rich in Si and Fe and poor in Al (Trendall, 2002). Proposed primary minerals are hydrous, Fe–silicate gels of greenalite-type composition, hydrous Na-, K- and Al-containing gels approximating stilpnomelane compositions, SiO_2 gels, $Fe(OH)_2$ and $Fe(OH)_3$ precipitates, and very fine-grained carbonate oozes of variable composition (Klein, 2005). However, recently, Rasmussen

* Corresponding author. Tel.: +86 10 82998185; fax: +86 10 62010846.
E-mail address: lczhang@mail.iggcas.ac.cn (L. Zhang).

http://dx.doi.org/10.1016/j.precamres.2014.08.002
0301-9268/

et al. (2013) postulated from petrographic examination of the ~2.5 Ga Brockman Iron Formation that iron silicate microgranules composed of stilpnomelane, which derived from chamosite or nontronite, were the precursor iron-rich components in BIFs. Rare earth element (REE), oxygen and Nd isotopic signatures suggest that the iron and silica in BIFs were mainly derived from the leaching of basalt and komatiites in the ocean floor by hydrothermal fluids, which then mixed with bulk ferrous seawater (Bau and Möller, 1993; Kato et al., 1998; Bekker et al., 2010); whereas Ge/Si ratios in BIFs have been used to infer a continental source for silica (Hamade et al., 2003).

BIFs can be divided into the Algoma-type and Superior-type on the basis of the sedimentary and tectonic environments in which they were deposited (Gross, 1980, 1996). The former are relatively small in size and thickness, and are often formed in arc/back-arc basins or intracratonic rift zones with a close affiliation with mafic/ultramafic to felsic volcanic rocks or volcaniclastic rocks and greywackes, whereas the latter, which are associated with clastic-carbonate rocks, are larger and their deposition occurred in relatively shallow marine conditions under transgressing seas, perhaps on the continental shelves of passive tectonic margins or in intracratonic basins. Despite the clear geological difference between the Algoma-type and Superior-type BIFs, some BIFs occurring in the transition area between the continental shelves and deep-water regions are identified as the transition type of BIFs (González et al., 2009).

As Precambrian marine sediments, the REE and isotopic compositions of BIFs have been used as proxies for understanding atmospheric evolution, the chemical composition of the ancient oceans, and the appearance of life. In China, the Anshan-Benxi, eastern Hebei, Wutai and Lüliang areas constitute most of the areas containing BIFs in the North China Craton (NCC). The BIFs have generally been metamorphosed to amphibolite facies and display strong deformational features. They occur not only in the greenstone belts but also in high-grade regions. Many researchers have focused primarily on the geology, geochemistry and tectonic settings of these BIFs (Zhai and Windley, 1990; Windley, 1995; Shen et al., 2009; Li et al., 2010a; X. J. Zhang et al., 2011; Zhang et al., 2012a; Dai et al., 2012; Wan et al., 2012a; Zhai and Santosh, 2013). In summary, the BIFs in the NCC possess three distinct characteristics: (1) Most of the BIFs are Archean in age with a peak in Neoarchean, except for the BIFs in the Lüliang areas that formed in the Paleoproterozoic (Geng et al., 2008; Liu et al., 2012). (2) The BIFs are generally formed in the island arc or back-arc basins (Zhang et al., 2012b). (3) Iron oxide, silica oxide, and silicate are predominant in nearly all the BIFs, with rare carbonates and sulfides.

The Wutai greenstone belt (WGB), situated in the central part of the NCC (Fig. 1a), is perhaps the best preserved granite-greenstone terrane in the NCC (Bai, 1986). The WGB comprises a sequence of metamorphosed ultramafic to felsic volcanic rocks, variably deformed granitoid rocks, along with lesser amounts of siliciclastic and carbonate rocks and BIFs. Although much attention has recently been given to the source of the BIF components (Li, 2008; Li et al., 2010b; Zhang et al., 2010), the genetic relationship between classical greenstone belt sequences in Precambrian cratons and concomitant BIFs is yet a conundrum. In this regard, we have investigated the composition of the Wangjiazhuang BIF in the Wutai Group exposed in the western part of the WGB (Fig. 1b). We present information on field occurrence, mineral and textural arrangements of the BIF. The geological information is complemented with major and trace elements whole-rock geochemical analyses on the BIF and associated lithologies and electron probe microanalytical data (EPMA) on main minerals of the BIF. In addition, we present the U–Pb zircon age of the interbedded amphibolites, which places constraints on the depositional age of the Wangjiazhuang BIF. Within the context of all these data, we discuss the timing of sedimentation of the BIF, its paragenesis and depositional environment, tectonic setting, and genetic relationship with coeval volcanism.

2. Geological background

2.1. Regional geology

The NCC consists of Archean to Paleoproterozoic metamorphic basement overlain by Mesoproterozoic to Cenozoic unmetamorphosed cover. The basement of the NCC can be divided into the Eastern and Western Blocks and the intervening Trans-North China Orogen (TNCO) (Zhao et al., 2005). Zhao et al. (2001) suggested that the TNCO was a Paleoproterozoic collisional orogen, along which the Eastern and Western Blocks were amalgamated to form the NCC at ~1.85 Ga. The Hengshan–Wutai–Fuping belt is situated in the middle segment of the TNCO (Fig. 1a) and consists of three distinct tectonic complexes: the upper amphibolite to granulite facies Fuping and Hengshan complexes in the southeast and northwest, respectively, separated by the greenschist- to lower amphibolite-facies Wutai Complex (Fig. 1), which is interpreted as a typical granite-greenstone belt (Bai, 1986; Tian, 1991; Bai et al., 1992).

The WGB consists of Neoarchean to Paleoproterozoic granitic plutons and metamorphosed volcanic and sedimentary rocks, traditionally named the Wutai and Hutuo Groups in the Chinese literature (Fig. 2). The granitoid plutons can be largely divided into three distinct types (Tian, 1991): the pre-, syno- and post-orogenic granites.

Based on lithologies and metamorphic grades, the Wutai Group is subdivided into three subgroups: Shizui, Taihuai and Gaofan Subgroups. The Shizui Subgroup consists of peridotite, oceanic tholeiite, dacite, rhyolite, chert, BIFs, sandstone, siltstone and minor limestone metamorphosed in amphibolite facies (Zhao et al., 2007). The Taihuai Subgroup comprises felsic volcanic rocks, BIFs and tholeiites metamorphosed in greenschist facies. The Gaofan Subgroup contains conglomerates, quartz greywackes, siltstones, limestones, and minor mafic to felsic volcanic rocks metamorphosed in subgreenschist facies. The Wutai Group is unconformably overlain by the Hutuo Group, which is composed of metasedimentary rocks, including conglomerate, quartzite, phyllite, slate, dolomitic marble, and local volcanic rocks. Rocks of this group are mostly metamorphosed in subgreenschist facies.

2.2. Geology of the Wangjiazhuang BIF

The WGB lithological assemblage is among the fertile settings for gold (Luo et al., 1999), VMS (Li et al., 2004; Niu et al., 2009), and iron ore deposits of Archean age. There are three important BIFs-bearing lithologic sequences, that are the lower part of the Jingangku Formation and the upper part of the Wenxi Formation in the Shizui Subgroup, the base of the Bozhiyan Formation in the Taihuai Subgroup (Fig. 2). The Wangjiazhuang BIF, located in the western part of the Yuanping city, is one of representative BIFs in the Jingangku Formation.

The exposed strata in this area include Neoarchean metamorphic sedimentary rocks of the Zhuangwang and Jingangku Formations in the Shizui Subgroup, and Paleozoic Cambrian-Ordovician carbonate rocks and shales (Fig. 3). The Zhuangwang and Jingangku Formations have similar lithological assemblages, which are composed mainly of biotite-hornblende leptynite, mica schist and amphibolites. The Wangjiazhuang BIF is distributed nearly in an E–W direction, extending 8 km in length and 0.5 km in width, and dips to the SE with a steep angle of 60°–80°. The tight homoclinal folding is widely developed in the strata resulting from multi-phase tectonic activities, which have had important effects

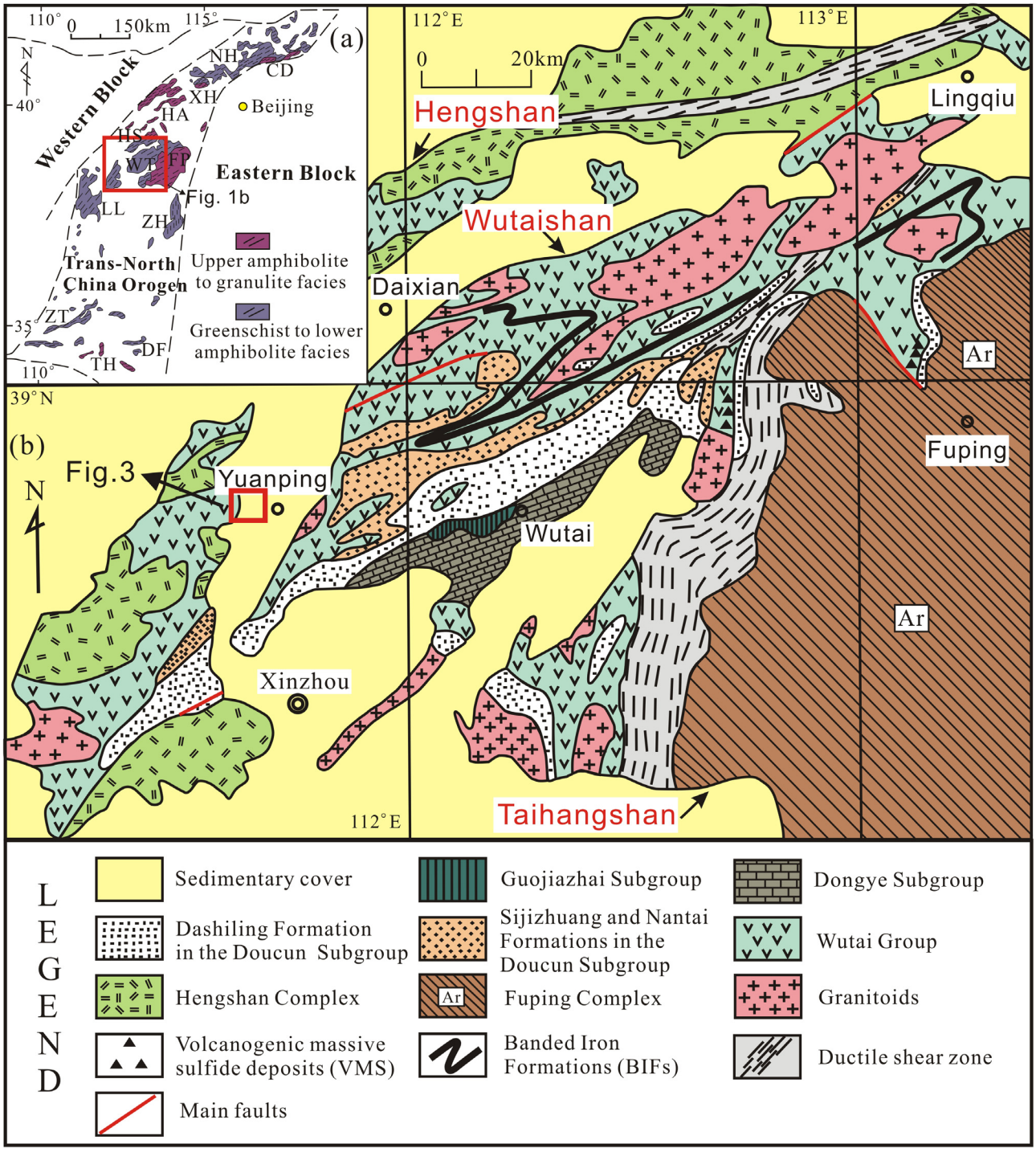

Fig. 1. (a) Regional geological sketch showing the location of the Hengshan–Wutai–Fuping belt in the North China Craton (revised after Zhao et al., 2005). Abbreviations for metamorphic complexes: CD, Chengde; DF, Dengfeng; FP, Fuping; HA, Huai'an; HS, Hengshan; LL, Lüliang; NH, Northern Hebei; TH, Taihua; WT, Wutai; XH, Xuanhua; ZH, Zanhuang; ZT, Zhongtiao. (b) Geological map of the Wutai greenstone belt.
Modified after Niu and Li (2006).

on constraining shapes of the BIF. In addition, there are two series of post-depositional brittle fractures based on different strikes (NE and NW directions), among which, the NW normal faults have had impacts on the destruction of the BIF.

Igneous rocks exposed in the area consist of granitic gneiss, trondhjemite, meta-basic rocks and metagabbro. The Wangjiazhuang granitic gneiss (Wgn), located in the northern part of the Wangjiazhuang BIF, is flesh pink-pale gray, medium-grained and inhomogeneous, consisting predominantly of plagioclase, K-feldspar, quartz and biotite. Toward the south of the field area, coarse-grained metagabbro terminates the BIF zone, and it displays strong schistosity with a linear amphibole-fabric orientated in the direction of the stretching. In addition, the remnants of the Fuping TTG gneiss are also exposed. They are pale gray, rather homogenous, non-migmatitic and consist mainly of granodioritic gneiss.

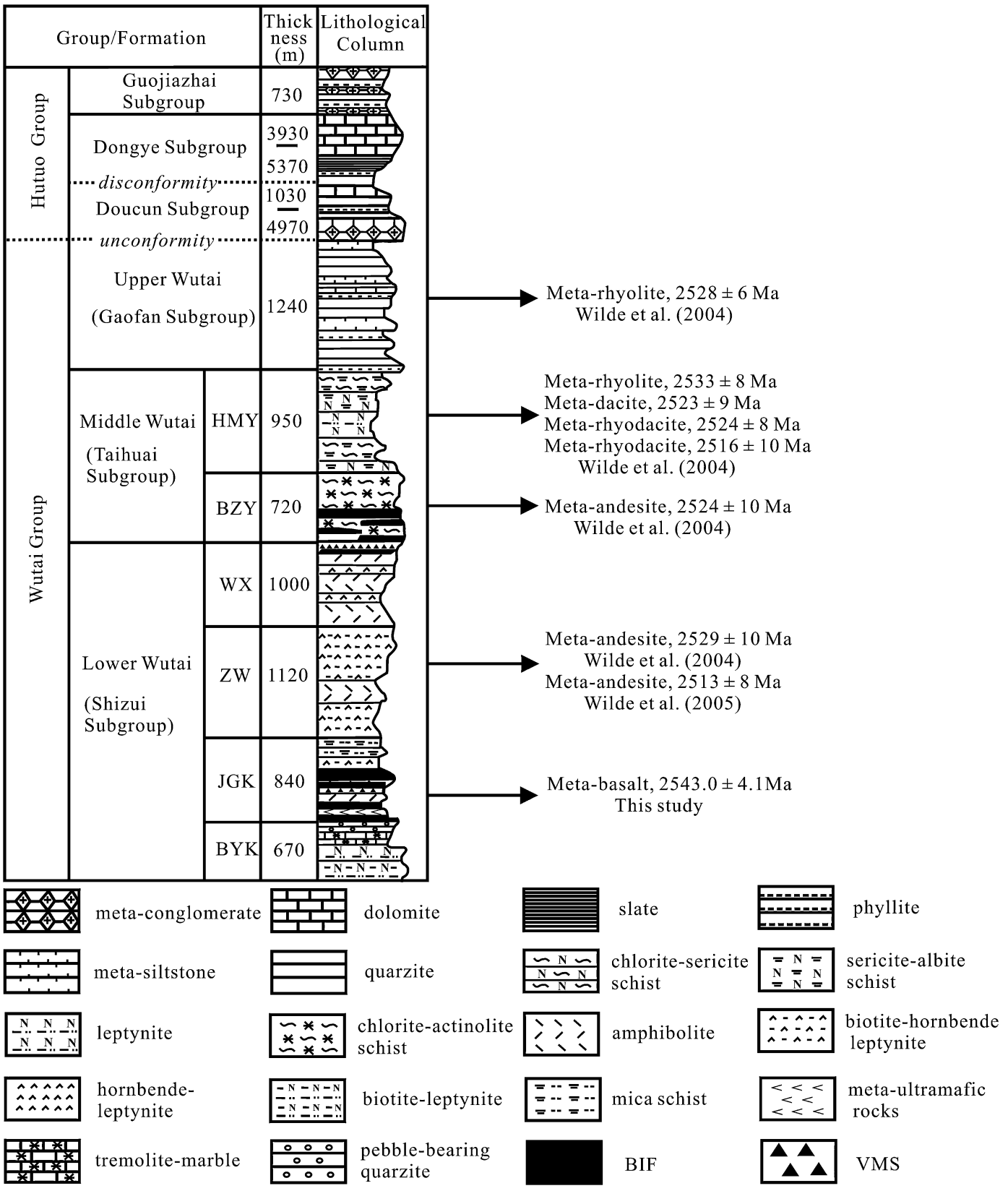

Fig. 2. Stratigraphic column showing group and formation names for different rock assemblages in the Wutai greenstone belt (modified after Kusky and Li, 2003). Abbreviations for formation names: BYK, Banyukou Formation; JGK, Jingangku Formation; ZW, Zhuangwang Formation; WX, Wenxi Formation; BZY, Baizhiyan Formation; HMY, Hongmenyan Formation.

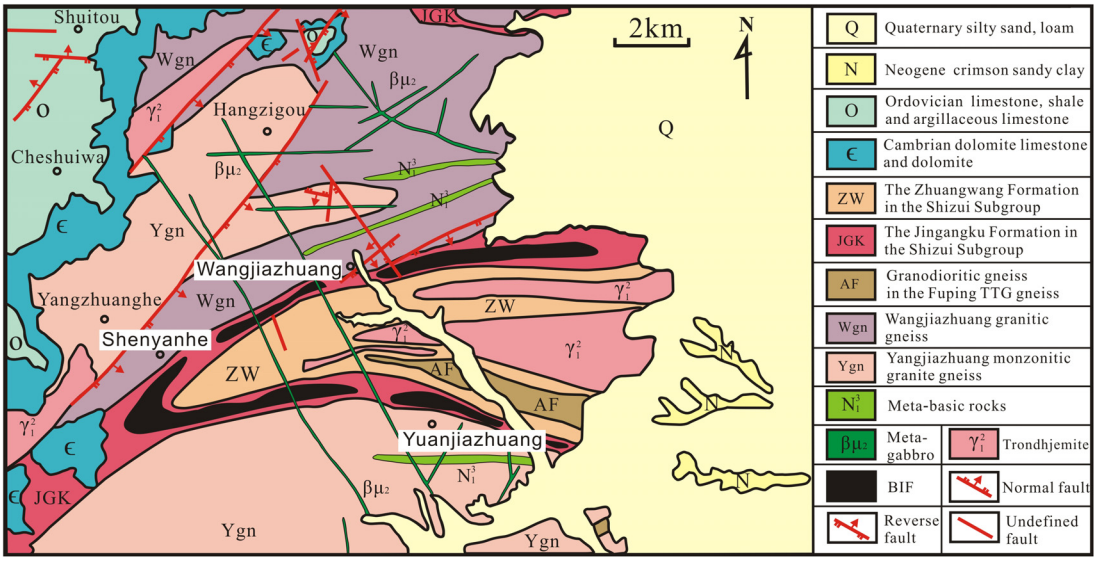

Fig. 3. Geological map of the Wangjiazhuang BIF.

Modified after Li (2008).

3. Sampling and analytical procedures

3.1. Field observation and sampling

Detailed field observation for the Wangjiazhuang BIF has focused on profiles of three ore blocks, including the Wangjiazhuang, Shenyanhe, and Yuanjiazhuang ore blocks (Fig. 3). These outcrops and sketch profiles are presented in Figs. 4a, b and 5. The lamination and banding of the BIF do not reflect the primary sedimentary bedding because of the post-depositional complex tectonometamorphism, which has gone up to middle-upper amphibolite facies (Zhao et al., 1999). Most of the BIF is deformed and primary layering is extensively transposed into a new tectonic layering or extended parallel to the plunge of the regionally dominant folds and associated lineations (Fig. 3). The thickness of the single-layer BIF ranges from 7 to 10 m, with greater thickness occurring in the Shenyanhe ore blocks due to tight homoclinal folding. Although weathered surfaces do occur locally, the whole BIF is generally fresh and unweathered. The main laminations of the BIF are intercalated with amphibolites and minor leptynite, and the contacts between amphibolites and the BIF, leptynite and the BIF are sharp, straight, and well-defined with no sign of any grading, erosion or intermixing (Fig. 4c and d). Occasionally, the BIF appears as a thin lens shape (Fig. 4e) and is characterized by weak bending deformation (Fig. 4f), whereas amphibolites and leptynite display stronger schistosity along the edge of the BIF, and far away from the BIF, the shistosity becomes weak. A few subsequent quartz or felsic veins penetrate into amphibolites and laminations of the iron formation, displaying dextral shearing characteristics (Fig. 6a). A lithological transformation can be found in the Wangjiazhuang BIF, generally varying from the BIF, amphibolites outward to leptynite, mica schist (Fig. 5).

Based on previous field observations, only samples from the least altered and deformed outcrops were obtained, including bulk-BIF samples and associated rocks (amphibolites, hornblende leptynite, biotite leptynite and mica schist). Especially for amphibolites occurring as concordant layers within the Wangjiazhuang BIF, they have the potential of providing a definitive depositional age for the BIF.

3.2. Analytical procedures

Detailed petrographic examination using transmitted and reflected light was carried out to determine the mineralogy and paragenesis of all samples. Electron microprobe analyses (EMPA) for the BIF samples were performed using a JEOL JXA-8100 electron microprobe operating at 15 kV and 20-nA current with a focused 31-μm electron beam, at the Institute of Geology and Geophysics, Chinese Academy of Sciences in Beijing.

Major elements for the bulk-BIF samples were determined using a PW2404 X-ray fluorescence spectrometer with an analytical error of less than 5% at the Analytical Laboratory at the Beijing Research Institute of Uranium Geology, and the FeO content was obtained by chemical titration. In addition, the rest of geochemical analyses were taken at the Institute of Geology and Geophysics, Chinese Academy of Sciences in Beijing. Major element oxides were analyzed using XRF-1500 X-ray fluorescence (XRF) with RSD between 0.1 and 1%. Trace element concentrations were analyzed with an inductively coupled plasma-mass spectrometer (ICP-MS) (Element, Finnigan MAT) using solution methods. The accuracy on the measured concentrations is within 5–10%.

Shale-normalized REE patterns (subscript "SN", normalized to the Post-Archean Australian shale (PAAS), after McLennan, 1989) are used for all bulk-BIF samples. Because Yttrium's chemical behavior is similar to those of the REE, Y is inserted between Dy and Ho based on its ionic radius. Thus, Y and the REE are described together (Henderson, 1984; Bau and Dulski, 1996, 1999). The La-anomaly was obtained by the procedure proposed by Bolhar et al. (2004): $(La/La^*)_{SN} = [La/(3Pr - 2Nd)]_{SN}$, whereas the Eu-anomaly was calculated as $(Eu/Eu^*)_{SN} = [Eu/(0.67Sm + 0.33Tb)]_{SN}$. REE for the non-BIF lithologies were chondrite- and primitive mantle-normalized according to Sun and McDonough (1989).

Prior to the U–Pb dating, zircon grains were separated from crushed amphibolite samples using heavy liquids and a Frantz magnetic separator. To investigate internal structures of the zircon grains, cathodo-luminescence (CL) images were taken using a CAMECA electron microprobe at the Institute of Geology and Geophysics, Chinese Academy of Sciences in Beijing. Uranium, Th and Pb isotopes were then analyzed by means of the Cameca SIMS-1280 ion microprobe, following the operating processes and

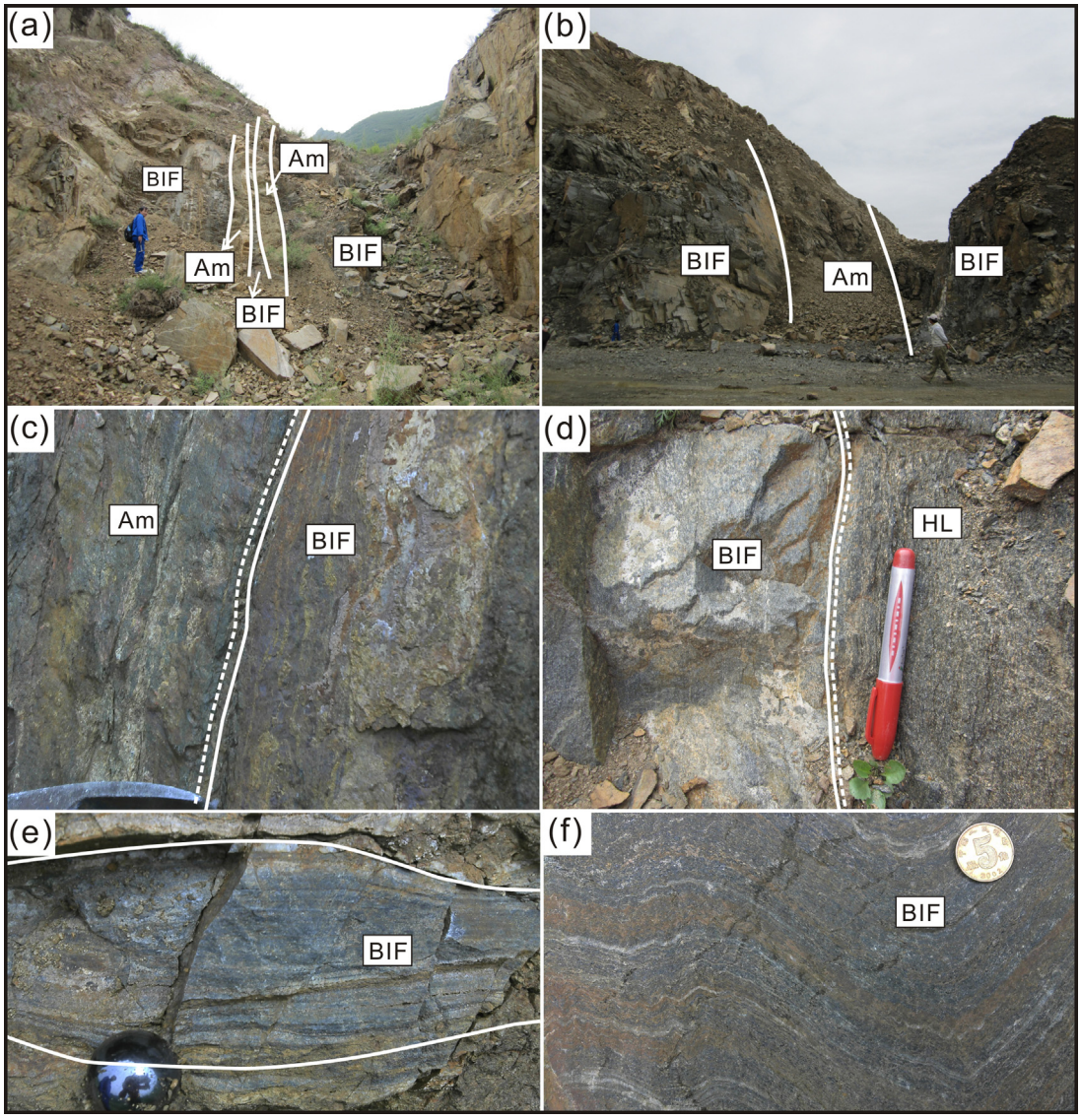

Fig. 4. Field photos of the Wangjiazhuang BIF. (a and b) Outcrops of the Wangjiazhuang, Shenyanhe geological profiles, showing a steep occurrence and interlayered amphibolites. (c and d) A sharp contact between the BIF and amphibolites (Am), the BIF and hornblende leptynite (HL). (e) Thin lens-shaped beds of the BIF, suggesting the BIF has undergone relatively strong compressional deformation. (f) Bending deformation of the BIF, showing the very fine laminae of quartz (white) and magnetite (black).

calculation described in detail by Li et al. (2009). A common-Pb correction was carried out based on the interference- and background-corrected ^{204}Pb signal and a model Pb composition (Stacey and Kramers, 1975). Uncertainties on individual analysis in data tables are reported at a 1σ level; mean ages for pooled U/Pb (and Pb/Pb) analyses are quoted with 95% confidence interval. The data were plotted using the software ISOPLOT (Ludwig, 2001).

4. Petrography

4.1. The banded iron formation and its mineral chemistry

The iron formation consists of alternating fine-grained Fe-rich and Si-rich micro- and mesobands ranging from less than 1 mm to 4 mm in width. These two types of bands are often straight and continuous (Fig. 6b), although the bending deformation is occasionally visible. The iron-rich bands are black, highly magnetic, whereas the Si-rich bands are white and generally finely laminated with a few bands of magnetite. Contacts between these two types of microbands are usually sharp (Fig. 6b), but more diffuse transitions within the Si-rich laminae are observed. The mineralogy of the Wangjiazhuang BIF varies both in contents and proportions due to slightly different mineral assemblages among the samples, for example, some samples are characterized by anomalously high amounts of garnet (up to 10%). The modal mineral abundances are quartz (40–50%), magnetite (20–30%), amphibole (25–30%), minor garnet (1–5%), pyrite (<1%) and calcite (<2%) (Figs. 6 and 7).

4.1.1. Magnetite

Magnetite is the main Fe-oxide mineral component of the Wangjiazhuang BIF, occurring as a dominant constituent of Fe-rich microbands (>60 modal %) and as a minor constituent of Si-rich microbands (<15 modal %). In both units, magnetite crystals occur as subhedral to anhedral grains typically between 60 and 300 μm in size, and they are scattered as individual grains or are interconnected to form irregular aggregates (Fig. 6c–e). It is obvious that most magnetite grains are found both in grain-boundary contact with and as inclusions in grains of grunerite, ferropargasite and quartz (Figs. 6f and 7e).

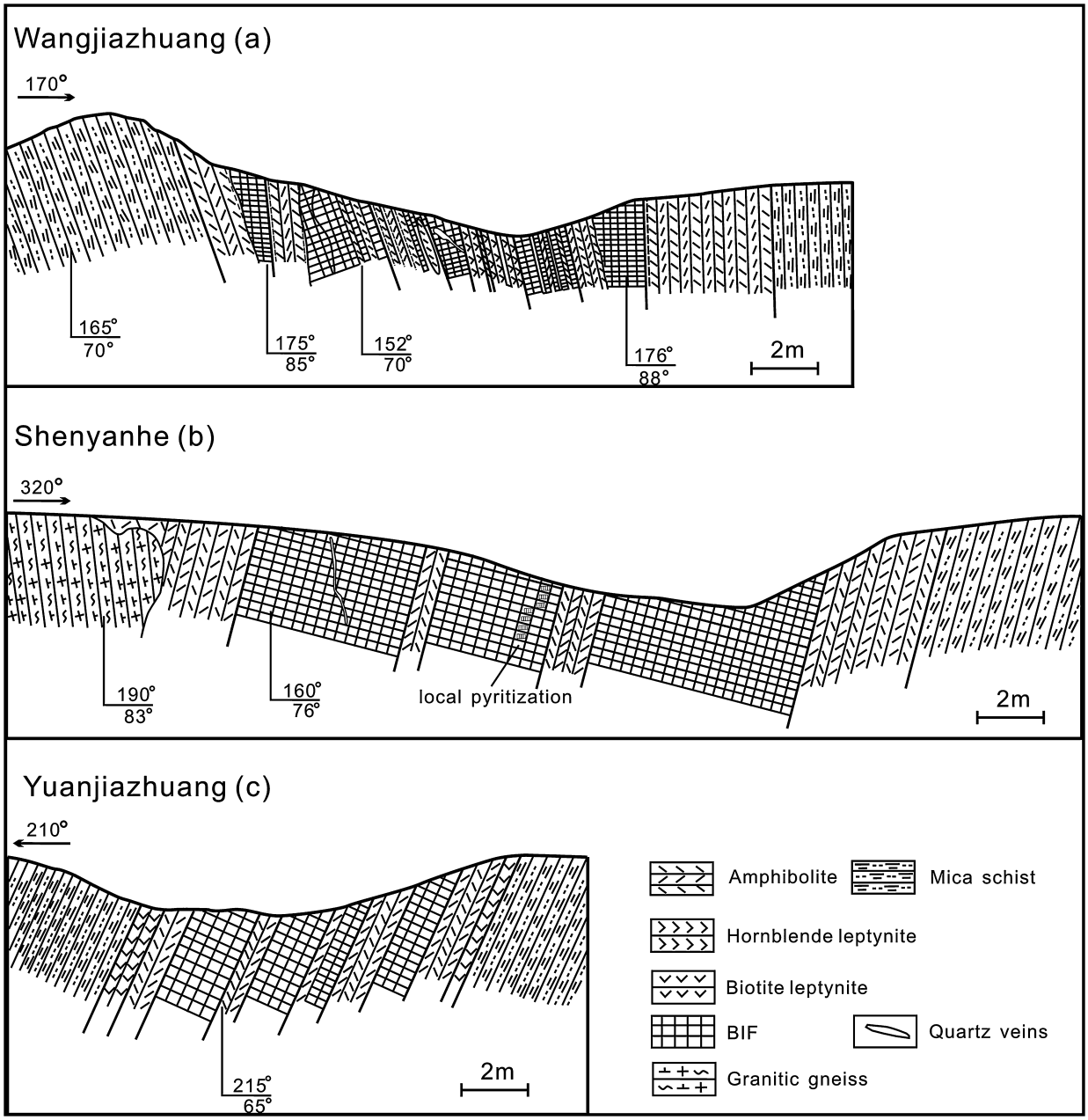

Fig. 5. Sketch profiles from the Wangjiazhuang BIF, showing relationships between the BIF and associated lithologies.

Electron probe microanalyses of magnetite in the Wangjiazhuang BIF indicate that the magnetite contains the highest Fe (wt%), between 87.91 and 93.16% (Table 1). In contrast to magnetite in some other iron formations, such as the Shuichang (Zhang et al., 2011) and Waitoushan (Dai et al., 2012) BIFs in China, it has high Al_2O_3 (average of 0.29%) and TiO_2 (average of 0.23%).

4.1.2. Quartz

As the most abundant mineral phase, quartz grains are subhedral-anhedral with 0.1–1.5 mm in size. Quartz occurs as microbands and as individual grains or irregular aggregates within the amphibole and magnetite microbands (Fig. 6c–e), although some individual grains or aggregates crosscut the banding. Occasionally, some quartz grains are found as inclusions within grains of amphibole (Fig. 7e). A typical polygonal granoblastic texture is defined by quartz with undulatory extinction, straight to curved boundaries and triple junctions, suggesting a late stage static recrystallization under temperature-dominated conditions (Fig. 6f).

4.1.3. Grunerite

Grunerite tends to be noticeably smaller in size, varying from 50 to 200 μm, occurring as subhedral to enhedral grains. Grunerite often composes microbands that alternate with quartz microbands or occurs as individual grains associated with magnetite or minor ferro-pargasite and calcite (Figs. 6e, f and 7d, e).

Grunerite is commonly found in rocks derived from regional metamorphism of Ca-poor and Fe- and Mg-rich protoliths (Deer et al., 1992), such as an iron formation (Table 2). The Mn content of grunerite varies between 0.057 and 0.113 apfu, which is accompanied by low Ca (0.073–0.165 apfu), Al (0.042–0.174 apfu) and a high bulk Fe# (FeO/FeO+MgO) > 0.40. These characteristics indicate that the iron formation has been affected by the medium-grade regional metamorphism (González et al., 2009).

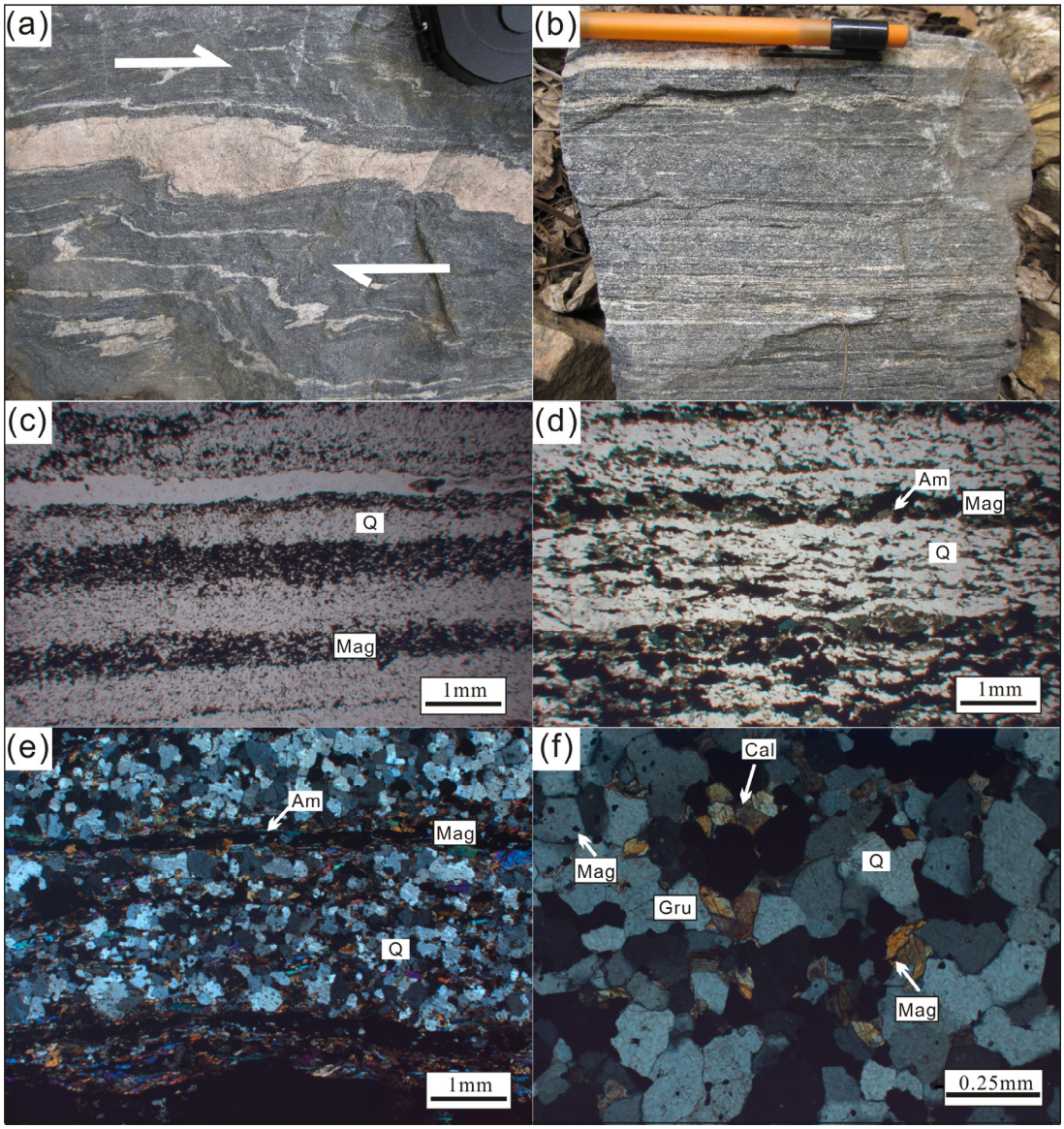

Fig. 6. Field photos of amphibolites and the BIF, including (a) and (b). (a) Amphibolites penetrated by later felsic veins, showing dextral shearing characteristics. (b) the Wangjiazhuang BIF composed of black magnetite-rich and white quartz-rich microbands, showing a sharp contact between these two units. Photomicrographs showing representative textures and petrographic relationships between the main mineral phases in the BIF, including (c–f). (c) BIF containing a simple mineralogy having only quartz (Q) (55–60%), magnetite (Mag) (30–35%) and minor amphibole (Am) (<5%) (plain-polarized light). (d) BIF consisting of alternating Fe-oxide (magnetite) and quartz bands, and amphibole associated with magnetite (plain-polarized light). (e) BIF consisting of alternating Fe-oxide (magnetite), amphibole and quartz bands (between crossed polarizers). (f) Quartz bands showing mineral grains relationships between magnetite, grunerite (Gru), quartz and calcite (Cal) (between crossed polarizers).

4.1.4. Ferro-pargasite

Ferro-parasite is often intergrown with both grunerite and magnetite (Fig. 7e). It occurs as individual, 50–400 μm large, anhedral to subhedral grains, commonly with inclusions of quartz and magnetite. In addition, it is also interconnected to be large aggregates. Along the edge of a few of garnet, some ferro-parasite exists as replacement minerals.

Major element analyses for ferro-parasite reveal that the two-type ferro-parasites (the scattered (I) and replacement minerals (II)) have similar compositions except for the Al_2O_3 and MgO concentrations (Table 2). The former is significantly more enriched in MgO and more depleted in Al_2O_3 than those of the latter, which are attributed to aftermentioned garnet compositions.

4.1.5. Ferro-actinolite

Ferro-actinolite was only observed in quartz microbands. As a minor component, it is only closely associated with grunerite, and occurs as a metasomatism product of grunerite (Fig. 7f).

In contrast to grunerite, ferro-actinolite has higher Al_2O_3 and CaO contents, and lower FeO content (Table 2).

4.1.6. Garnet

Garnet is associated with the quartz bands and occurs most commonly as idioblastic to sub-idioblastic, near-equiaxed, individual grains (I) (up to 2.0 mm) with minor magnetite inclusions (Fig. 7a). It is often replaced by surrounding ferro-pargasite. In addition, another form of garnet (II) was found, occurring as long lath-shaped grains with small ilmenite inclusions (Fig. 7b). Its length varies between 0.5 and 2.5 mm (Fig. 7c). These garnet grains have been

Table 1
Electron probe microanalyses of magnetite from the Wangjiazhuang BIF.

Content (wt%)	Na_2O	SiO_2	Cr_2O_3	SO_3	MgO	MnO	Cl	Al_2O_3	P_2O_5	FeO	K_2O	NiO	CaO	ZnO	TiO_2	Total
1	0.00	0.05	0.00	0.00	0.00	0.05	0.01	0.15	0.00	92.91	0.00	0.07	0.07	0.00	0.17	93.47
2	0.02	0.02	0.08	0.03	0.00	0.00	0.02	0.19	0.00	92.88	0.01	0.00	0.05	0.02	0.44	93.74
3	0.05	0.13	0.01	0.03	0.02	0.04	0.02	0.23	0.00	92.43	0.00	0.00	0.07	0.00	0.04	93.07
4	0.08	0.13	0.03	0.04	0.00	0.00	0.00	0.47	0.00	92.87	0.00	0.04	0.00	0.00	0.05	93.70
5	0.07	0.09	0.05	0.00	0.04	0.02	0.02	0.42	0.05	92.86	0.00	0.00	0.00	0.00	0.05	93.64
6	0.08	0.09	0.02	0.07	0.03	0.00	0.00	0.38	0.00	92.64	0.00	0.05	0.02	0.02	0.00	93.40
7	0.12	0.02	0.08	0.02	0.00	0.04	0.00	0.41	0.00	92.52	0.00	0.08	0.03	0.00	0.00	93.32
8	0.11	0.12	0.01	0.00	0.00	0.00	0.04	0.37	0.03	92.45	0.01	0.00	0.01	0.00	0.09	93.24
9	0.05	0.18	0.01	0.00	0.02	0.00	0.00	0.38	0.00	91.89	0.00	0.00	0.03	0.04	0.05	92.65
10	0.10	0.07	0.00	0.01	0.00	0.03	0.03	0.42	0.00	91.83	0.00	0.05	0.01	0.04	0.00	92.58
11	0.07	0.08	0.06	0.00	0.00	0.00	0.00	0.40	0.00	93.16	0.00	0.05	0.03	0.00	0.00	93.85
12	0.00	0.07	0.01	0.00	0.02	0.01	0.00	0.38	0.00	92.87	0.00	0.00	0.00	0.00	0.04	93.40
13	0.02	0.03	0.00	0.01	0.00	0.00	0.01	0.39	0.00	92.42	0.00	0.01	0.03	0.00	0.00	92.93
14	0.00	0.01	0.03	0.00	0.06	0.06	0.02	0.35	0.01	91.83	0.00	0.07	0.03	0.02	0.05	92.54
15	0.06	0.00	0.04	0.00	0.01	0.11	0.03	0.32	0.07	89.33	0.00	0.00	0.05	0.00	0.01	90.01
16	0.00	0.06	0.02	0.02	0.04	0.03	0.00	0.30	0.01	92.29	0.00	0.00	0.05	0.01	0.01	92.83
17	0.00	0.06	0.07	0.03	0.00	0.07	0.00	0.26	0.00	92.07	0.00	0.00	0.05	0.00	0.88	93.49
18	0.05	0.12	0.05	0.00	0.03	0.02	0.00	0.19	0.01	93.11	0.00	0.00	0.00	0.00	0.49	94.06
19	0.00	0.07	0.05	0.00	0.02	0.08	0.02	0.29	0.00	92.85	0.00	0.05	0.02	0.00	0.12	93.56
20	0.00	0.15	0.04	0.00	0.00	0.00	0.01	0.20	0.00	93.09	0.02	0.00	0.04	0.00	0.11	93.66
21	0.00	0.13	0.05	0.00	0.00	0.00	0.00	0.29	0.37	87.91	0.00	0.07	0.53	0.00	0.84	90.17
22	0.00	0.21	0.05	0.02	0.00	0.05	0.01	0.17	0.01	89.22	0.00	0.02	0.04	0.00	0.37	90.16
23	0.01	0.12	0.04	0.04	0.00	0.04	0.01	0.20	0.00	92.86	0.00	0.00	0.01	0.00	0.21	93.53
24	0.03	0.16	0.03	0.00	0.00	0.05	0.00	0.19	0.00	93.11	0.00	0.00	0.00	0.04	0.24	93.84
25	0.04	0.07	0.03	0.00	0.06	0.07	0.00	0.27	0.00	93.10	0.00	0.00	0.01	0.01	0.74	94.41
26	0.06	0.10	0.07	0.00	0.00	0.06	0.00	0.20	0.00	92.72	0.00	0.01	0.02	0.08	0.53	93.85
27	0.05	0.12	0.07	0.00	0.04	0.01	0.00	0.16	0.09	92.04	0.00	0.02	0.03	0.03	0.59	93.23
min	0.00	0.00	0.00	0.00	0.00	0.00	0.00	0.15	0.00	87.91	0.00	0.00	0.00	0.00	0.00	90.01
max	0.12	0.21	0.08	0.07	0.06	0.11	0.04	0.47	0.37	93.16	0.02	0.08	0.53	0.08	0.88	94.41
average	0.04	0.09	0.04	0.01	0.01	0.03	0.01	0.29	0.02	92.19	0.00	0.02	0.05	0.01	0.23	93.05

broken off into a few of fragments because of late-stage bending deformation seen from the surrounding quartz and grunerite microbands, whereas the very fine lamellae of grunerite within garnet is straight, which represents early bedding (Fig. 7c and d). These two-type garnets can also be found in one sample.

Similar major element compositions for the two-type garnets reveal that they are almandine rich (Xalm = 0.774–0.857), with higher content of spessartine (Xspess = 0.017–0.037) than pyrope (Xpyr = 0.121–0.032) and grossular (Xgros = 0.075–0.157) content, and an almost constant XFe that varies between 0.867 and 0.964 (Table 2). With regard to the undeveloped zonal structure of garnet, the each individual cation content does not vary significantly in some internal locations, which suggests that garnet was possibly homogenized during peak metamorphic conditions. Spear (1993) argued that garnets usually reach typical almandine-rich homogeneous compositions only when attaining high amphibolites facies. Based on this, the studied garnet must have undergone this medium-grade metamorphism. Compared with the composition of the metasomatic ferro-pargasite, the I-type garnet lack contents of Na_2O and K_2O, indicating that a minor amount of external Na^+ and K^+ should be required for this replacement.

4.2. Amphibolites

The amphibolites are typically dark-green or dark-gray, fine-grained, locally medium-grained rocks. They form several concordant intercalations some tens of decimeters thick scattered in the Wangjiazhuang BIF. Magmatic textures and minerals have been completely eradicated by metamorphism. The rocks usually exhibit a moderate- to weakly developed foliation and, in some instances, a mineral lineation (Fig. 8a and b). They are composed dominantly of amphibole (60–65%), plagioclase (25–30%), and lesser amounts of quartz (<5%) and biotite (<5%). Anhedral to subhedral amphibole grains in most of the samples share a moderate to weak shape preferred orientation (Fig. 8b), spanning a varied range of sizes from 50 up to 1500 μm. Undulose quartz and plagioclase occur as scattered individual grains. Plagioclase sericitization is sporadic, and occasionally amphibole is replaced by biotite (Fig. 8c). Amphibolites are regarded as metamorphosed basaltic rocks in terms of the mineral assemblages and textures and previous work on their geochemistry (Zhao et al., 1999; Wang et al., 2004; Zhang et al., 2010).

4.3. Biotite/hornblende leptynite

Leptynites include two types: biotite leptynite and hornblende leptynite, which are often associated with amphibolites or minor BIF layers. The former is common, typically dark gray, and displays a fine-grained lepido-granoblastic texture and weakly developed foliation (Fig. 8d). It consists mainly of quartz (30–35%), feldspar (35–40%), biotite (15–20%) and minor amounts of garnet (<5%) and apatite (<2%). The quartz grains are generally angular to subangular, but a minor portion of the monocrystalline grains are spherical and well-rounded. Biotite often occurs as tabular crystals varying in size from 10 to 200 μm, and shows weak orientation. Fine- to medium-grained sub-angular feldspar with minor alteration is found throughout. The idioblastic garnet is poikiloblastic with scatteredly arranged quartz inclusions. The latter has similar texture and mineral assemblages to those of biotite leptynite. It is composed of quartz (30–35%), feldspar (30–35%), amphibole (20–25%) and minor amounts of biotite (<5%) and garnet (<2%) (Fig. 8e). The amphibole shows weak pleochroism, indicating low iron content. It occurs commonly as medium-grained (0.5–1 mm) subhedral grains, showing a preferred orientation. Considering large amounts of feldspar and relatively simple mineral phases observed in the leptynite, the protolith of leptynite should be a felsic volcanic rock (Bai, 1986).

4.4. Mica schist

The unit is most pronounced far away from the BIF zone, varying in thickness from tens of decimeters to tens of meters. It displays strong schistosity and comprises quartz (35–45%), biotite (15–20%),

Table 2
Electron probe microanalyses of grunerite, ferro-pargasite, ferro-actinolite and garnet from the Wangjiazhuang BIF.

	Grunerite											Ferro-pargasite				ferro-actinolite			Garnet			
(%)	1	2	3	4	5	6	7	8	9	10	11	I	II-1	II-2	II-3	1	2	(%)	I-1	I-2	II-1	II-2
SiO_2	51.224	51.431	50.945	50.762	51.657	51.047	50.838	50.600	49.643	49.741	52.418	41.341	38.969	40.007	39.566	50.799	51.149	SiO_2	37.460	37.920	37.960	35.152
TiO_2	0.051	0	0	0.008	0.021	0.004	0.025	0	0	0.012	0	0.351	0.271	0.515	0.046	0.008	0.067	TiO_2	0.060	0.100	0.079	0.074
Al_2O_3	0.829	0.708	0.617	0.661	0.520	0.255	0.206	0.371	0.172	0.176	0.154	10.894	13.262	13.050	12.579	1.739	1.550	Al_2O_3	20.620	20.820	20.845	20.340
Cr_2O_3	0.019	0	0	0	0.048	0	0.018	0	0.008	0.235	0.036	0.002	0.003	0.050	0	0.023	0.012	Cr_2O_3	0.080	0	0.0230	0.139
FeO	38.113	38.065	38.606	38.888	39.203	40.607	40.641	40.276	34.015	32.218	34.543	28.555	28.384	28.175	28.791	28.616	29.004	FeO	37.610	35.980	34.176	35.762
MnO	0.566	0.623	0.597	0.583	0.643	0.648	0.554	0.423	0.826	0.592	0.792	0.126	0.194	0.225	0.187	0.275	0.385	MnO	1.010	0.790	1.613	0.774
MgO	6.566	7.010	5.979	5.924	6.059	4.972	4.850	4.933	8.646	5.954	9.117	3.339	1.731	2.333	2.076	5.327	5.342	MgO	0.790	0.790	0.777	3.083
CaO	0.987	0.840	0.631	0.628	0.600	0.431	0.430	0.509	0.828	5.850	0.556	10.626	11.115	11.216	11.400	10.819	10.661	CaO	3.010	4.800	5.420	2.647
Na_2O	0.107	0.085	0.041	0.121	0.088	0.026	0.074	0.201	0.022	0.093	0	1.136	1.243	1.244	0.938	0.123	0.193	Na_2O	0.030	0	0.019	0
K_2O	0.017	0.017	0	0.005	0	0	0	0	0.032	0.047	0	1.246	1.232	1.076	1.303	0.098	0.072	K_2O	0	0	0	0
NiO	0.035	0	0.033	0.032	0	0.011	0	0	0	0.029	0.015	0.006	0	0.003	0	0.001	0	NiO	0.020	0	0	0
F	0	0	0	0	0	0	0	0	0	0	0	0	0	0	0	0	0	Total	100.690	101.210	100.912	97.971
Cl	0.014	0.009	0.026	0.008	0.002	0.017	0	0.038	0.004	0.019	0.011	0.101	1.037	0.780	0.745	0.093	0.093					
Total	98.528	98.788	97.475	97.620	98.841	98.018	97.636	97.351	94.196	94.966	97.642	97.723	97.441	98.674	97.631	97.921	98.528					
Cations per 23 oxygens																		Cations per 24 oxygens				
Si	7.997	7.997	8.000	8.000	8.000	8.000	8.000	8.000	8.000	8.000	8.000	6.571	6.304	6.344	6.376	7.863	7.877	Si	6.062	6.071	6.080	5.837
Al^{IV}	0.003	0.003	0.000	0.000	0.000	0.000	0.000	0.000	0.000	0.000	0.000	1.429	1.696	1.656	1.624	0.137	0.123	Ti	0.008	0.012	0.010	0.009
Sum T	8.000	8.000	8.000	8.000	8.000	8.000	8.000	8.000	8.000	8.000	8.000	8.000	8.000	8.000	8.000	8.000	8.000	Al	3.933	3.930	3.935	3.981
Al^{VI}	0.150	0.127	0.174	0.156	0.156	0.147	0.141	0.153	0.042	0.045	0.125	0.611	0.833	0.782	0.765	0.181	0.158	Sum Y+Z	10.003	10.013	10.024	9.827
Ti	0.006	0.000	0.000	0.001	0.002	0.000	0.003	0.000	0.000	0.001	0.000	0.042	0.033	0.061	0.006	0.001	0.008	Fe^{2+}	5.090	4.818	4.578	4.966
Mg	1.528	1.625	1.410	1.398	1.409	1.176	1.152	1.175	2.080	1.430	2.100	0.791	0.417	0.551	0.499	1.229	1.226	Mn	0.138	0.107	0.219	0.109
Fe^{2+}	4.975	4.949	5.107	5.146	5.115	5.388	5.416	5.380	4.589	4.339	4.462	3.795	3.840	3.736	3.880	3.704	3.735	Mg	0.190	0.189	0.186	0.763
Sum C	6.659	6.701	6.690	6.701	6.682	6.712	6.712	6.707	6.710	5.816	6.687	5.239	5.123	5.131	5.149	5.115	5.127	Ca	0.521	0.823	0.930	0.471
Mn	0.075	0.082	0.080	0.078	0.085	0.087	0.075	0.057	0.113	0.081	0.104	0.017	0.027	0.030	0.026	0.036	0.050	Na	0.008	0.000	0.006	0.000
Ca	0.165	0.140	0.107	0.106	0.100	0.073	0.073	0.087	0.143	1.009	0.092	1.809	1.926	1.905	1.968	1.794	1.759	K	0.001	0.000	0.000	0.000
Na	0.032	0.026	0.013	0.037	0.027	0.008	0.023	0.062	0.007	0.029	0.000	0.000	0.000	0.000	0.000	0.037	0.058	Sum X	5.947	5.937	5.918	6.309
Sum B	0.272	0.248	0.199	0.222	0.212	0.168	0.171	0.207	0.263	1.119	0.196	1.826	1.953	1.935	1.994	1.867	1.867					
Na	0.000	0.000	0.000	0.000	0.000	0.000	0.000	0.000	0.000	0.000	0.000	0.416	0.466	0.455	0.436	0.000	0.000	Pyrope	0.032	0.032	0.031	0.121
K	0.003	0.003	0.000	0.001	0.000	0.000	0.000	0.000	0.007	0.010	0.000	0.253	0.254	0.218	0.268	0.019	0.014	Alman	0.857	0.811	0.774	0.787
Sum A	0.003	0.003	0.000	0.001	0.000	0.000	0.000	0.000	0.007	0.010	0.000	0.668	0.720	0.673	0.704	0.019	0.014	Gros	0.088	0.139	0.157	0.075
Mg#	0.230	0.250	0.220	0.210	0.220	0.180	0.180	0.180	0.310	0.250	0.320	0.173	0.100	0.130	0.110	0.250	0.250	Spess	0.023	0.018	0.037	0.017
Fe#	0.770	0.750	0.780	0.790	0.780	0.820	0.820	0.820	0.690	0.750	0.680	0.827	0.900	0.870	0.890	0.750	0.750	XFe	0.964	0.962	0.961	0.867

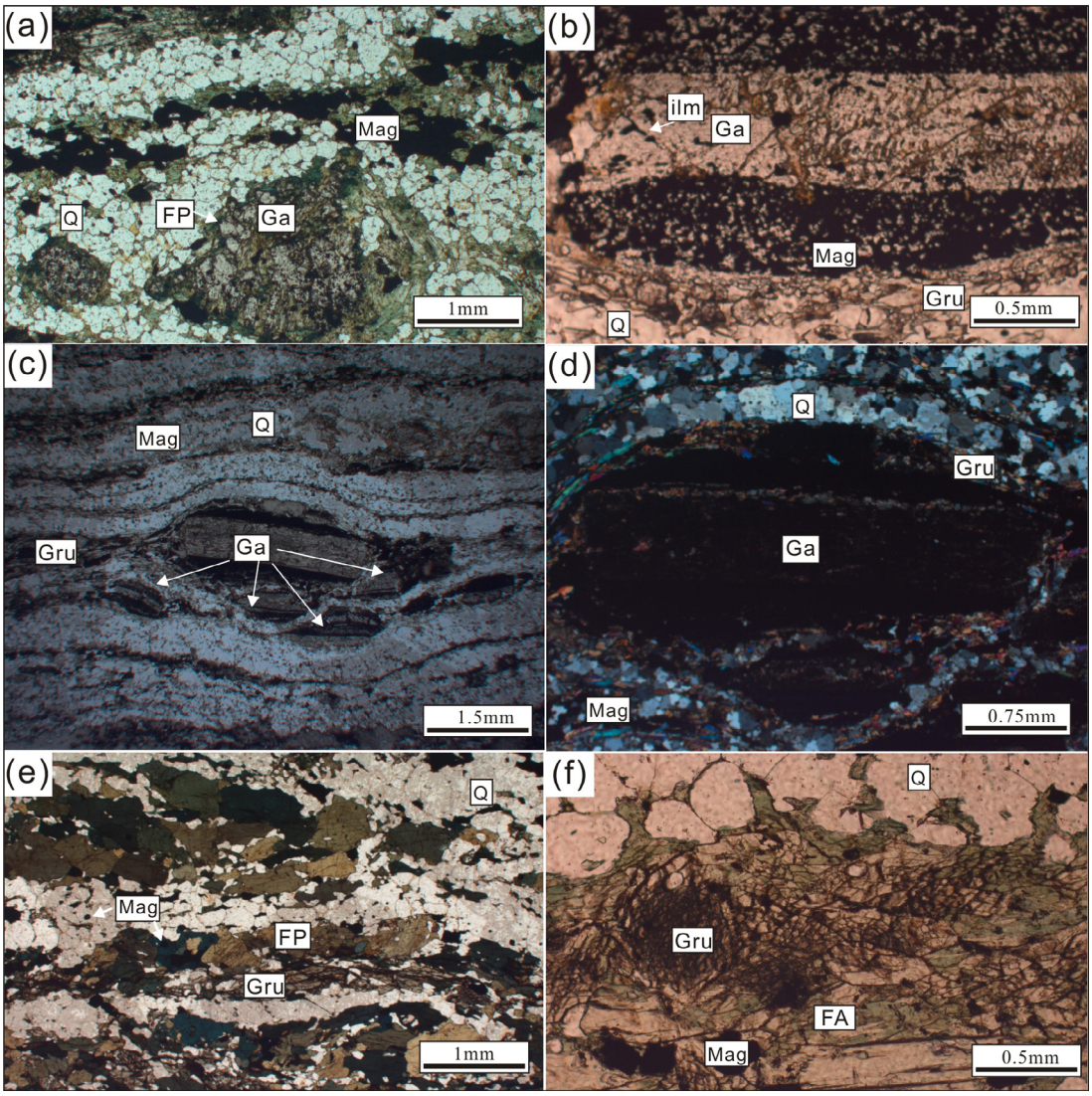

Fig. 7. Micro-photographs showing the mineralogy and typical textures of the Wangjiazhuang BIF. (a) Scattered garnet (Ga) grains in quartz (Q) microbands replaced by surrounding ferro-pargasite (FP), with some magnetite (Mag) inclusions (plain-polarized light). (b) Lath-shaped garnet grains containing little ilmenite, surrounded by magnetite, quartz and grunerite (Gru) (plain-polarized light). (c) The alternating bands of BIF showing weak bending deformation, which has resulted in the breakdown of lath-shaped garnet (plain-polarized light). (d) Very fine lamella of grunerite within garnet showing the straightness, although grunerite and quartz microbands are curved (between crossed polarizers). (e) Quartz bands showing mineral grains relationships between grunerite and ferro-pargasite (plain-polarized light). (f) Subhedral grunerite grains in quartz microbands replaced by ferro-actinolite (plain-polarized light).

muscovite (15–20%), feldspar (15–20%), and minor garnet (<5%) (Fig. 8f). Quartz occurs as subhedral-anhedral grains with minor undulatory extinction. Biotite and muscovite often forms continuously elongated flakes with weak flexure, displaying a preferred crystallographic orientation. Occasionally, the cross hatched- and polysynthetic twin can be observed in alkali feldspar and plagioclase, respectively (Fig. 8g). The diablastic garnet (up to 2.5 mm) contains inhomogeneously distributed quartz, biotite and opaque mineral inclusions (Fig. 8h). Bai (1986) and Li (2008) interpreted mica schist as metapelite in terms of its geochemical and mineralogical characteristics.

5. Geochronological and geochemical results

5.1. Geochronological results

Based on previous microscopic structure and geochemical characteristics of amphibolites in the WGB (Zhao et al., 1999; Wang et al., 2004; Zhang et al., 2010), we suggest that the Wutai amphibolites have a volcanic or subvolcanic origin. As concordant intercalations in the Wangjiazhuang BIF, amphibolites provide a synchronous age with the BIF. Zircon grains from the amphibolite samples analyzed in this study are euhedral to subhedral with 60–200 μm in length and greater length to width ratios (up to 5) (Fig. 9a). The majority of these zircons are either colorless or brown, and they are prismatic grains with a clear oscillatory magmatic zoning, which are typical features of zircon crystallized from a melt. Furthermore, most of them lack tiny zircon overgrowth rim, suggesting that late-stage processes such as metamorphism have little effects on initial zircon.

Spot analyses for U, Th and Pb were carried out on 14 zircon grains, resulting in Th/U ratios between 0.43 and 1.35, which are values typical of magmatic zircons (Table 3). They define a discordia line with an upper intercept age of 2543.0 ± 4.1 Ma (Fig. 9b) and a weighted mean $^{207}Pb/^{206}Pb$ age of 2542.5 ± 3.1 Ma (Fig. 9c), which we interpret as the formation time of the amphibolite protolith based on the following three reasons: (1) Careful heavy mineral separation using 5–6 kg of sample material yielded

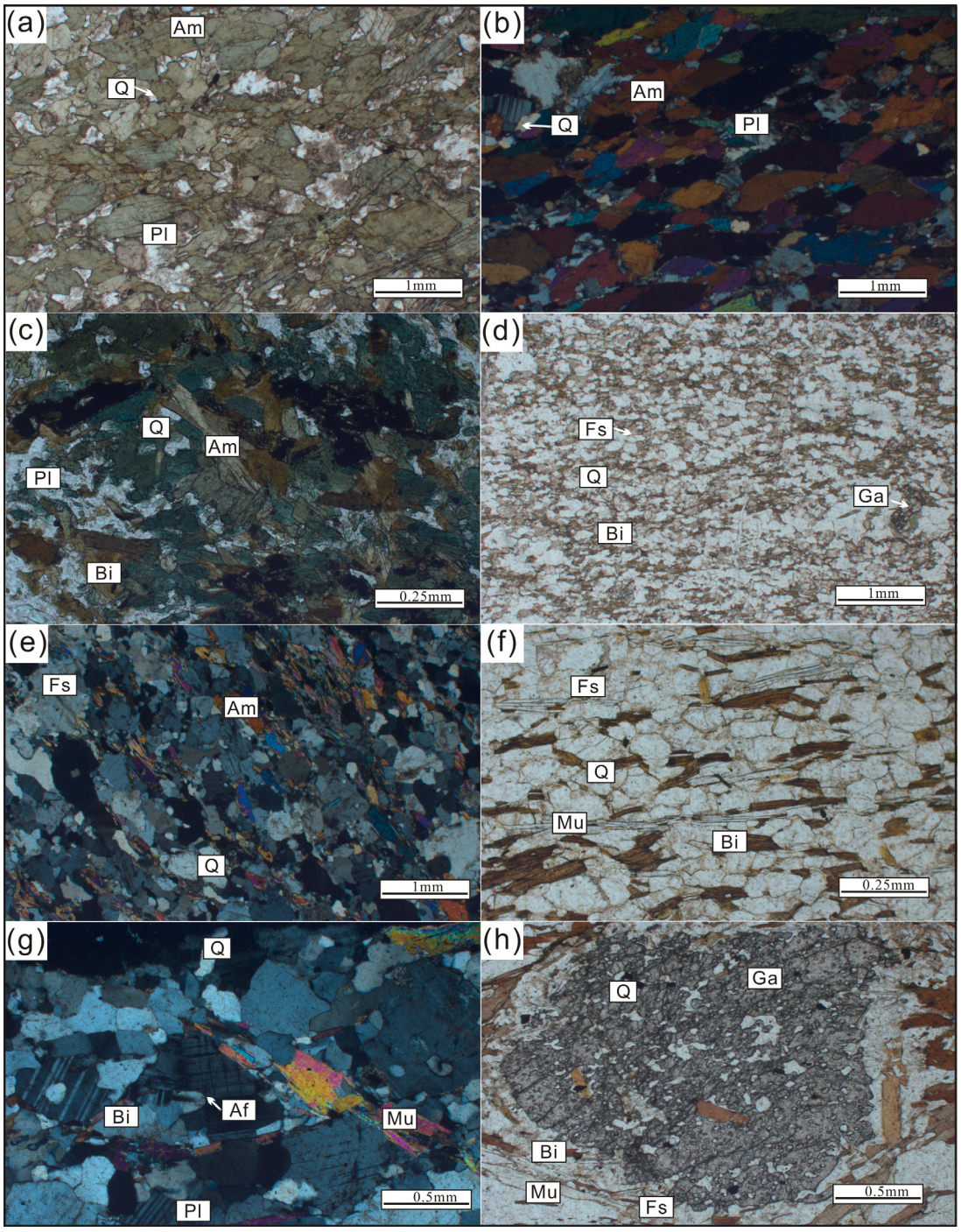

Fig. 8. Micro-photographs of lithologies associated with the Wangjiazhuang BIF. (a) Amphibolites composed of anhedral to subhedral amphibole (Am), unaltered plagioclase (Pl) and minor quartz (Q) (plain-polarized light). (b) Amphibole in amphibolites showing a moderate to weak shape preferred orientation (between crossed polarizers). (c) Subhedral amphibole grains in amphibolites replaced by tabular biotite (Bi) (plain-polarized light). (d) Biotite leptynite comprising angular to sub-angular quartz, fresh feldspar (Fs), tabular biotite and minor garnet (Ga), showing weakly developed foliation defined by biotite (plain-polarized light). (e) Hornblende leptynite composed of quartz, feldspar and lath-shaped amphibole, displaying granoblastic texture (between crossed polarizers). (f) Mica schist comprising quartz, feldspar, biotite, muscovite (Mu) (plain-polarized light). Flexural mica shows a preferred crystallographic orientation. (g) Two-type feldspar in mica schist (between crossed polarizers). Not the twinning in plagioclase and alkali feldspar (Af), respectively. (h) Diablastic garnet in mica schist containing quartz, biotite and opaque mineral inclusions (plain-polarized light).

exceedingly low abundances of zircon grains, generally fewer than 200 grains. (2) All spot analyses on 14 random zircons give a concentrated $^{207}Pb/^{206}Pb$ age spectrum. (3) This age is slightly older than those of overlying meta-volcanics. In addition, previous studies (Kröner et al., 2006; Liu et al., 2012, and references therein) indicate that typical magmatic zircons can be crystallized from basaltic magma, which is in accord with the above conclusion.

5.2. Geochemical results

5.2.1. Banded iron formation

Concentrations of major elements and selected trace elements in the Wangjiazhuang BIF are displayed in Table 4. The major oxide components in the BIF are Fe_2O_3 (all iron as Fe^{3+}) and SiO_2, ranging from 31.67 to 49.43% and 43.67 to 55.19%, respectively. Similar abundances are observed among Al_2O_3 (0.62–4.78%),

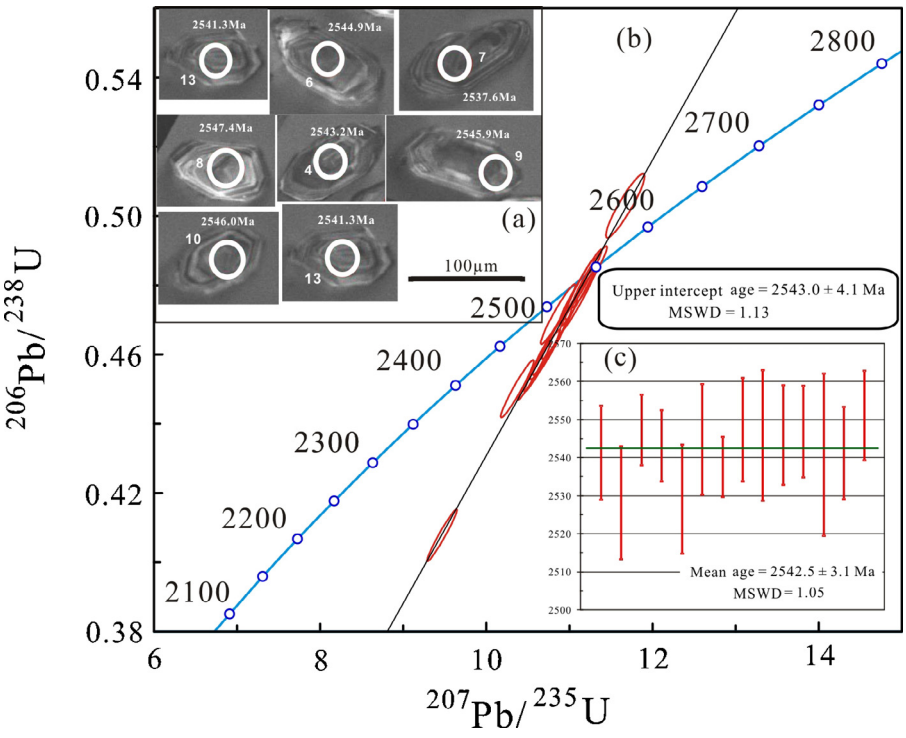

Fig. 9. Concordia diagram of SIMS zircon U–Pb data from amphibolites associated with the Wangjiazhuang BIF, including cathodoluminescence (CL) images of zircon grains from amphibolites analyzed in this study.

MgO (1.54–3.07%) and CaO (2.25–4.99%). The other major element oxides occur in concentrations less than 0.5%, such as TiO_2 (0.02–0.16%). In terms of incompatible elements, Hf and Th have average concentrations of <1 ppm; whereas Sc and Zr have higher average concentrations of 2.59 ppm and 9.38 ppm, respectively.

The total REE and Y concentrations (ΣREY) of all samples are high, ranging from 23.59 to 45.62 ppm. Shale-normalized REE patterns of the Wangjiazhuang BIF (Fig. 10) are characterized by positive La anomalies (0.95–1.38) and Eu anomalies (1.41–3.08), LREE and MREE depletion relative to HREE ($(La/Yb)_{SN} < 1$; $(Sm/Yb)_{SN} < 1$).

5.2.2. Amphibolites

The Zr/TiO_2-Nb/Y diagram is used to constrain types of volcanics in the WGB (Winchester and Floyd, 1977). Amphibolites and leptynites plot within the basalt and dacite-rhyolite fields, respectively (Fig. 11). Amphibolites show low contents of SiO_2 (48.45–52.83%) and TiO_2 (0.65–1.33%), whereas the concentration of MgO varies from 5.38 to 9.12% (Table 5). REE patterns display slight LREE depletion relative to HREE or near-flat chondrite normalized patters with $(La/Yb)_N$ ratios of 0.80–1.09, characterized by weak negative Ce anomalies ($\delta Ce = 0.76–0.91$) and no Eu anomalies ($\delta Eu = 0.93–1.04$) (Fig. 12a). On a primitive mantle normalized diagram (Fig. 12b), it shows intense Th and slight Nb, La, Zr, Ti, and Y negative anomalies.

These meta-basalts (amphibolites) have characteristics similar to those of N-MORB (Sun and McDonough, 1989), which are characterized by depletion in Th, Nb and La, nearly flat or LREE-depleted REE patterns, and greater Nb/U and Nb/Th ratios relative to those of primitive mantle. However, nearly flat trace-element patterns with Ti and Y troughs are also observed in meta-basalts samples, which are typical features of back arc basin basalt (BABB) (Ghazi et al., 2012; Zhang et al., 2013). An interaction between MORB-like melts and subduction-related melts might be responsible for these characteristics of basalts, suggesting that they were probably formed in a back arc basin setting. In addition, the Zr/Hf ratios (26–33) of amphibolites are lower than those of modern N-MORB (36, see Sun and McDonough, 1989). The systematic variations of Zr/Hf ratios in these rocks can be used to indicate an original magmatic feature. These lower ratios can also be attributed to MORB-like melts imprinted by subduction-related melts (Wang et al., 2004).

5.2.3. Leptynites

Leptynites (meta-felsic volcanics) show a range of SiO_2 from 58.32 to 69.90%, Al_2O_3 from 12.48 to 16.75%, MgO from 1.04 to 3.46% (Table 5). On REE and primitive mantle normalized diagrams (Fig. 12c and d), leptynites are characterized by systematically: (1) moderate LREE enrichment relative to HREE; (2) weak to moderate negative Eu anomalies; (3) negative Nb, Nd, Ti, and Y anomalies. The depletion of Eu may have resulted from either plagioclase fractionation or retention of plagioclase as a residual phase in the source. Flat to depleted HREE patterns of these felsic volcanics suggest that they were derived partial melting of N-MORB-like oceanic crust. And the observed LREE-enriched, and Nb- and Ti-depleted characteristics indicate that this partial melting of the oceanic crust took place at <80 km under the influence of subduction zone processes (Pearce and Peate, 1995; Polat et al., 2005).

5.2.4. Mica schist

The SiO_2, Al_2O_3, and MgO contents of these meta-pelites vary between 63.71 and 74.61%, 14.20 and 17.07%, 0.56 and 1.95%, respectively (Table 5). On the chondrite-normalized and primitive mantle normalized diagrams (Fig. 12c and d), pelites display similar characteristics with that of felsic volcanics, such as LREE enrichment, negative Nb, Ti anomalies, which suggest that pelites may derived from the weathering of felsic source similar to above-mentioned felsic volcanics.

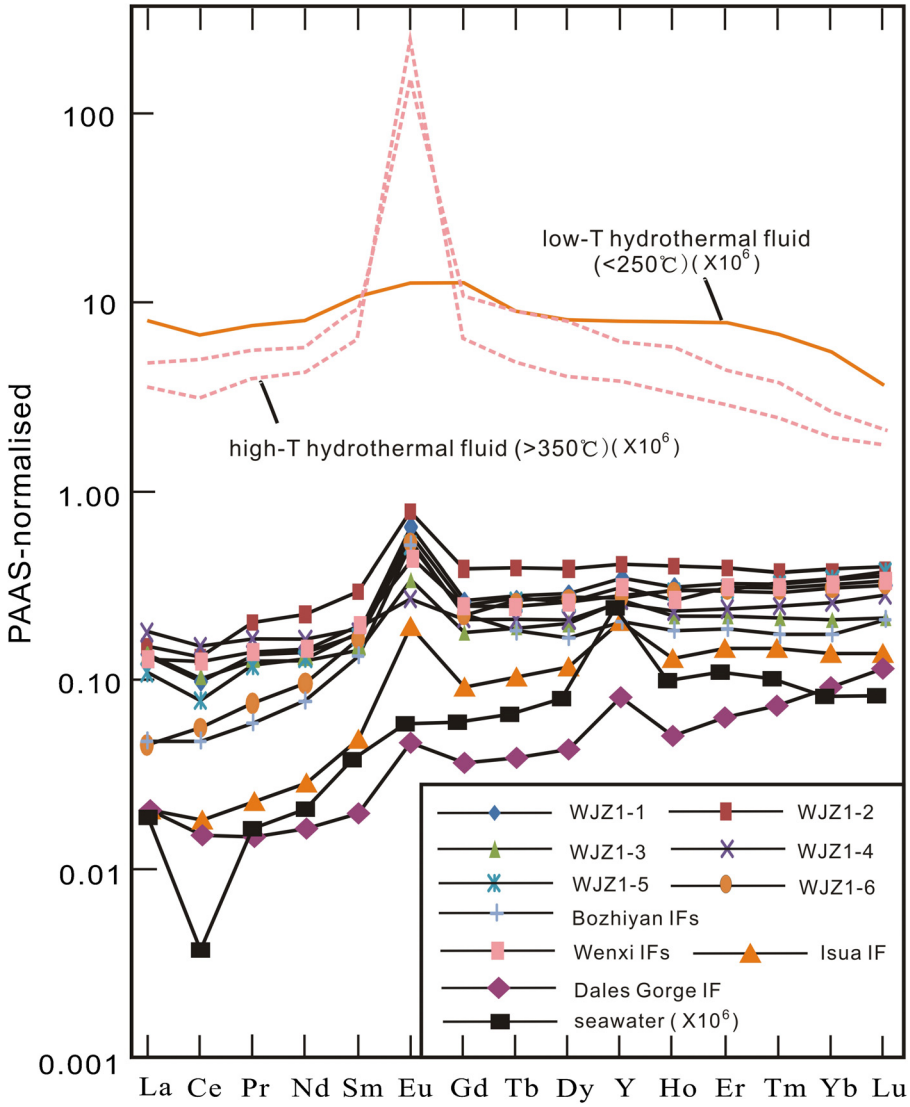

Fig. 10. REY distributions of the Wangjiachuang BIF, average IFs in the Wenxi and Bozhiyan Formations, average Dales Gorge and Isua IFs, as well as average high-T (>350 °C) and low-T (<250 °C) hydrothermal fluids, average South Pacific seawater. Data from Li et al. (2010a); Pecoits et al. (2009); Bolhar et al. (2004); Bolhar and Van Kranendonk (2007).

6. Discussion

6.1. Paragenesis

The petrographic and mineralogical study of the Wangjiazhuang BIF allows us to simply establish different stages of mineral genesis and assess the diagenetic modification of the likely primary minerals. However, it is difficult for us to identify the mineral phases in BIFs exactly considering that primary minerals are much smaller, far less common, and have been modified due to subsequent processes, such as diagenesis and metamorphism (Bekker et al., 2010). The present mineral assemblage of the Wangjiazhuang BIF is a typical amphibolite-facies equilibrium assemblage (Klein, 2005), which is composed predominantly of quartz, magnetite, grunerite, ferro-pargasite, garnet and minor calcite.

Most authors agree that BIFs are chemical sediments influenced by contaminated materials carried by rivers or winds or deposited by volcanic activity (Isley, 1995; Kato et al., 1998). The abundances of Al_2O_3 and TiO_2, typically related to clastic detritus or volcanic debris, can be used to reveal contamination degrees. The Al-rich mineral phases such as garnet and ferro-pargasite are observed

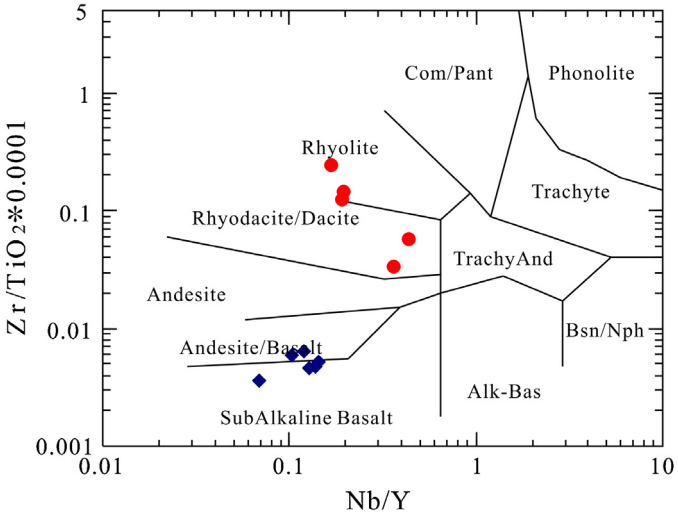

Fig. 11. Diagram of Zr/TiO_2 vs. Nb/Y (Winchester and Floyd, 1977) for volcanic rocks associated with the Wangjiazhuang BIF. Diamonds = amphibolites; circles = leptynite.

Table 3
SIMS U–Pb analytical results of zircon from amphibolites associated with the Wangjiazhuang BIF.

Sample spot	U (ppm)	Th (ppm)	Pb (ppm)	Th/U	f_{206}[a] %	$^{207}Pb/^{235}U$	±σ (%)	$^{206}Pb/^{238}U$	±σ (%)	$^{207}Pb/^{206}Pb$	±σ (%)	$^{207}Pb/^{206}Pb$	±σ (Ma)	$^{207}Pb/^{235}U$	±σ (Ma)	$^{206}Pb/^{238}U$	±σ (Ma)
WJZ2-1-1	142	191	77	1.35	0.16	9.4667	1.55	0.4078	1.50	0.1684	0.37	2541.4	6.2	2384.3	14.3	2204.9	28.1
WJZ2-1-2	77	46	48	0.60	0.05	10.8636	1.56	0.4717	1.50	0.1670	0.44	2528.2	7.4	2511.5	14.7	2490.9	31.1
WJZ2-1-3	188	181	129	0.96	0.01	11.1141	1.53	0.4771	1.50	0.1690	0.28	2547.4	4.7	2532.7	14.3	2514.5	31.3
WJZ2-1-4	206	148	127	0.72	0.01	10.5775	1.53	0.4552	1.51	0.1685	0.28	2543.2	4.7	2486.7	14.3	2418.2	30.5
WJZ2-1-5	118	80	69	0.68	0.15	10.3721	1.56	0.4501	1.50	0.1671	0.43	2529.1	7.2	2468.6	14.6	2395.7	30.1
WJZ2-1-6	117	78	71	0.66	0.03	10.7913	1.78	0.4639	1.73	0.1687	0.43	2544.9	7.3	2505.3	16.7	2456.8	35.4
WJZ2-1-7	261	208	173	0.80	0.01	11.0943	1.53	0.4790	1.51	0.1680	0.24	2537.6	3.9	2531.1	14.3	2522.9	31.6
WJZ2-1-8	91	51	58	0.56	0.04	11.2384	1.56	0.4824	1.50	0.1690	0.41	2547.4	6.8	2543.1	14.6	2537.7	31.6
WJZ2-1-9	148	83	90	0.56	0.02	10.7459	1.65	0.4617	1.56	0.1688	0.52	2545.9	8.6	2501.4	15.4	2447.0	31.9
WJZ2-1-10	99	78	63	0.79	0.03	10.8815	1.59	0.4675	1.54	0.1688	0.39	2546.0	6.5	2513.1	14.9	2472.5	31.6
WJZ2-1-11	133	77	81	0.58	0.19	10.6720	1.65	0.4582	1.61	0.1689	0.36	2546.9	6.0	2495.0	15.4	2431.7	32.7
WJZ2-1-12	107	47	69	0.43	0.02	11.6713	1.63	0.5029	1.50	0.1683	0.64	2540.9	10.7	2578.4	15.4	2626.4	32.5
WJZ2-1-13	141	75	89	0.53	0.02	11.1754	1.56	0.4814	1.52	0.1684	0.36	2541.3	6.1	2537.9	14.6	2533.6	31.8
WJZ2-1-14	151	87	95	0.58	0.01	11.0870	1.54	0.4748	1.50	0.1693	0.35	2551.1	5.9	2530.5	14.5	2504.8	31.3

[a] f_{206} is the percentage of common ^{206}Pb in total ^{206}Pb.

Table 4
Major elements (wt%) and selected trace elements (ppm) of the Wangjiazhuang BIF.

Sample	WJZ1-1	WJZ1-2	WJZ1-3	WJZ1-4	WJZ1-5	WJZ1-6
SiO_2	43.67	55.19	44.93	54.79	46.11	45.70
Al_2O_3	1.20	4.78	1.00	2.44	0.87	0.62
TFe_2O_3	47.99	31.67	44.65	35.50	47.82	49.43
MgO	1.95	1.84	3.07	2.98	1.79	1.54
CaO	2.28	4.99	4.04	3.20	2.81	2.25
Na_2O	0.07	0.35	0.27	0.02	0.09	0.07
K_2O	0.20	0.44	0.04	0.02	0.10	0.06
MnO	0.13	0.13	0.09	0.22	0.13	0.09
TiO_2	0.04	0.16	0.06	0.07	0.04	0.02
P_2O_5	0.16	0.14	0.14	0.10	0.18	0.18
LOI	1.79	<0.10	1.66	0.64	<0.10	<0.10
TOT	99.47	99.68	99.95	99.99	99.94	99.96
FeO	17.50	14.90	19.50	30.80	18.90	18.10
Li	6.24	6.09	1.88	1.86	1.26	1.46
Be	1.40	1.28	1.10	0.25	0.70	0.80
Sc	5.56	6.28	0.81	1.41	0.89	0.58
V	23.73	39.49	12.94	15.20	10.80	14.12
Co	9.50	11.72	2.80	4.20	2.95	2.28
Cu	47.84	132.50	12.04	2.76	19.59	13.23
Zn	69.97	85.14	23.91	26.22	66.64	42.17
Ga	4.23	9.41	2.33	3.22	2.43	2.32
Rb	9.38	10.15	1.73	4.07	9.25	7.03
Sr	43.51	26.36	20.17	14.21	23.84	30.47
Zr	7.72	21.27	3.97	15.58	4.86	2.87
Nb	1.62	2.59	1.01	1.39	1.16	1.14
Cs	1.28	1.18	0.43	0.37	0.94	1.30
La	5.27	5.73	5.09	6.76	4.13	1.71
Ce	7.81	10.41	8.24	11.84	6.14	4.36
Pr	1.12	1.77	1.15	1.45	1.03	0.66
Nd	4.77	7.50	4.54	5.48	4.34	3.22
Sm	0.99	1.63	0.84	1.00	0.92	0.91
Eu	0.69	0.84	0.37	0.29	0.55	0.57
Gd	1.21	1.79	0.84	0.97	1.10	1.03
Tb	0.21	0.30	0.15	0.16	0.20	0.20
Dy	1.33	1.81	0.93	0.97	1.20	1.24
Y	9.42	10.97	7.08	7.05	8.14	7.43
Ho	0.31	0.39	0.22	0.23	0.29	0.29
Er	0.87	1.11	0.62	0.67	0.86	0.85
Tm	0.12	0.15	0.09	0.10	0.13	0.12
Yb	0.87	1.06	0.59	0.72	0.96	0.86
Lu	0.14	0.17	0.09	0.12	0.16	0.14
Hf	0.26	0.73	0.12	0.48	0.14	0.10
Ta	0.04	0.20	0.06	0.10	0.06	0.06
Tl	0.09	0.07	0.00	0.01	0.04	0.02
Pb	2.10	2.21	2.72	1.17	0.82	0.87
Bi	0.73	1.14	0.04	0.00	1.02	0.13
Th	0.49	1.14	0.27	1.39	0.41	0.56
U	0.62	0.79	0.10	0.21	0.12	0.18
Th/U	0.79	1.44	2.83	6.52	3.33	3.15
Zr/Hf	29.58	29.18	32.85	32.41	35.29	28.28
Hf/Ta	6.07	3.65	2.19	4.81	2.15	1.74
$\sum$REE + Y	35.14	45.62	30.83	37.80	30.16	23.59
Y/Ho	30.69	27.92	32.88	31.05	28.12	25.66
$(La/Yb)_{SN}$	0.45	0.40	0.64	0.70	0.32	0.15
$(Sm/Yb)_{SN}$	0.58	0.78	0.72	0.71	0.49	0.54
$(La/La^*)_{SN}$	1.38	0.95	1.07	1.05	1.14	1.37
$(Pr/Pr^*)_{SN}$	1.07	1.14	1.10	1.06	1.14	0.99
$(Ce/Ce^*)_{SN}$	0.74	0.75	0.78	0.87	0.69	0.92
$(Y/Y^*)_{SN}$	1.17	1.04	1.26	1.20	1.10	0.98
$(Eu/Eu^*)_{SN}$	3.08	2.39	2.08	1.41	2.61	2.75

Total Fe reported as Fe_2O_3. $(Pr/Pr^*)_{SN} = [2Pr/(Ce + Nd)]_{SN}$; $(Ce/Ce^*)_{SN} = [2Ce/(La + Pr)]_{SN}$; $(La/La^*)_{SN} = [La/(3Pr - 2Nd)]_{SN}$; $(Eu/Eu^*)_{SN} = [Eu/(0.67Sm + 0.33Tb)]_{SN}$.

in the BIF, suggesting that the initial precipitates must have been affected by syn-depositional clastics.

As the main Fe-oxide mineral, magnetite can be found as inclusions within all the other minerals, which suggests that it was formed first among these minerals. It is very probable that ferric-oxyhydroxide was the precursor to magnetite (Ayres, 1972; Klein, 2005; Pecoits et al., 2009; Bekker et al., 2010). Large amounts of Fe (II) were required for the conversion from original ferric-oxyhydroxides to magnetite.

Table 5
Major elements and selected trace elements of lithologies associated with the Wangjiazhuang BIF.

Sample	Amphibolites						Hornblende leptynite			Biotite leptynite		Mica schist			
	WJZ2-2	WJZ2-3	WJZ2-4	WJZ2-5	WJZ2-6	WJZ2-7	WJZ3-1	WJZ3-2[a]	WJZ3-3[a]	WJZ4-1	WJZ4-2	WJZ5-1	WJZ5-2	WJZ5-3	WJZ5-4[a]
wt.%															
SiO_2	52.83	48.45	50.07	49.94	49.46	52.12	66.62	58.32	65.10	69.9	69.86	74.61	63.71	67.13	66.29
TiO_2	1.33	0.65	1.19	1.27	0.93	1.02	0.50	0.45	0.26	0.26	0.21	0.19	0.70	0.48	0.27
Al_2O_3	13.21	14.39	13.66	13.97	14.02	13.52	14.46	16.75	12.85	12.51	12.48	14.20	17.07	16.46	14.57
MnO	0.19	0.18	0.20	0.21	0.21	0.18	0.04	0.14	0.21	0.12	0.09	0.05	0.07	0.02	0.08
MgO	6.06	9.12	5.81	5.38	7.03	6.36	2.60	3.46	1.04	1.31	1.22	0.56	1.95	1.66	1.80
CaO	8.49	10.43	8.32	7.82	10.50	8.10	2.46	4.39	3.44	2.79	3.72	2.07	2.66	1.95	2.62
Na_2O	1.61	1.53	3.41	3.64	2.89	3.20	5.93	3.99	3.30	1.22	1.59	2.61	3.29	2.37	2.47
K_2O	0.19	0.30	0.53	0.50	0.63	0.69	0.32	1.84	0.66	2.46	2.4	2.04	2.75	3.21	1.89
P_2O_5	0.05	0.05	0.09	0.08	0.34	0.08	0.14	0.15	0.08	0.07	0.05	0.07	0.15	0.08	0.08
TFe_2O_3	14.66	11.82	15.24	15.62	12.54	13.64	6.46	7.70	11.44	7.98	6.53	2.39	6.42	4.35	7.40
LOI	0.94	1.99	0.70	0.78	0.84	0.60	0.44	1.48	0.10	1.72	2.20	1.26	1.16	2.60	1.72
Sum	99.56	98.91	99.22	99.21	99.39	99.51	99.97	98.67	98.48	100.34	100.35	100.05	99.93	100.31	99.19
ppm															
Li	15.40	18.72	8.24	9.36	13.60	19.21	4.76	11.10	20.30	31.94	31.78	10.04	30.82	25.78	27.10
Be	0.33	0.21	0.35	0.40	0.36	0.41	1.12	0.70	2.20	1.69	1.52	2.31	1.22	1.57	1.70
Sc	28.92	40.98	37.53	38.99	34.43	36.72	7.36			8.15	5.44	3.94	14.15	8.58	
V	211.01	211.50	226.08	240.95	221.00	213.00	88.93	97.60	19.00	11.89	7.36	22.24	113.84	74.00	18.90
Cr	269.83	673.96	250.01	205.56	203.00	238.00	234.67	62.40	8.60	315.34	212.09	349.70	322.42	243.50	10.10
Co	50.44	52.00	47.05	47.61	45.30	43.04	14.75	19.40	8.40	6.31	3.59	6.72	21.59	13.74	9.80
Ni	125.54	212.89	79.97	64.26	143.00	151.00	44.76	84.30	21.10	19.14	9.00	19.44	61.72	35.45	10.00
Cu	84.33	77.48	168.23	49.14	175.36	228.34	12.21	48.60	42.00	5.85	2.63	12.25	31.40	15.45	32.20
Zn	250.78	88.38	106.85	111.06	124.00	117.00	24.66	75.10	183.00	142.26	111.22	24.18	78.50	72.31	66.50
Ga	17.98	13.15	17.00	18.41	15.64	17.52	17.64			20.90	19.52	18.73	21.83	21.37	
Rb	3.02	9.90	9.06	10.76	10.35	17.30	11.32	51.30	22.60	94.61	82.99	65.69	64.76	55.47	99.50
Sr	101.39	81.90	165.90	133.77	189.30	123.32	322.07	208.00	94.00	133.78	148.15	198.68	211.67	203.22	167.00
Y	20.47	14.00	21.07	24.01	22.70	21.35	12.74	12.80	69.80	55.91	54.50	13.16	12.92	10.59	37.10
Zr	49.38	34.99	57.30	60.26	53.20	60.12	170.77	252.00	618.00	331.98	312.42	142.11	149.83	209.20	144.00
Nb	1.41	1.99	2.92	3.03	2.34	2.46	4.59	5.60	11.70	10.75	10.63	15.92	7.29	10.69	12.90
Cs	0.07	0.34	0.18	0.19	0.26	0.70	0.56	1.30	1.60	3.89	3.36	2.77	6.92	3.35	9.40
Ba	69.40	103.66	43.85	43.95	67.26	113.00	68.45	257.00	152.00	606.00	452.53	689.74	479.33	717.70	340.00
La	2.26	2.17	3.57	3.88	3.15	3.43	22.75	12.20	30.20	33.04	33.76	21.92	21.10	25.24	22.60
Ce	5.62	5.16	8.43	8.26	6.12	8.30	47.20	23.90	65.10	68.32	70.02	50.70	42.43	50.01	78.20
Pr	1.14	0.89	1.51	1.64	1.23	1.73	5.36	2.62	8.66	9.62	9.85	4.25	5.37	6.30	6.80
Nd	7.05	4.68	8.08	9.01	7.73	9.12	20.13	9.74	35.00	41.31	42.48	14.00	20.05	23.93	27.00
Sm	2.64	1.53	2.73	2.95	2.54	2.84	3.43	2.03	7.74	9.38	9.44	2.40	4.02	4.17	6.36
Eu	1.03	0.58	0.97	1.10	0.86	1.04	0.93	0.71	1.61	2.09	1.96	0.66	1.07	1.03	1.52
Gd	3.52	2.06	3.40	3.79	3.13	3.34	2.98	2.37	10.20	9.86	9.85	2.01	3.35	3.43	7.04
Tb	0.65	0.38	0.62	0.71	0.53	0.61	0.44	0.34	1.66	1.71	1.72	0.32	0.49	0.48	1.12
Dy	4.26	2.50	4.16	4.62	3.43	3.94	2.51	2.15	10.30	10.77	10.63	2.02	2.61	2.50	6.86
Ho	0.89	0.56	0.90	0.98	0.83	0.95	0.51	0.45	2.33	2.36	2.32	0.42	0.49	0.47	1.50
Er	2.32	1.62	2.42	2.70	2.48	2.63	1.37	1.39	7.00	6.54	6.42	1.26	1.32	1.24	4.64
Tm	0.32	0.25	0.37	0.41	0.34	0.43	0.20	0.20	1.05	0.98	0.95	0.20	0.19	0.18	0.68
Yb	2.03	1.67	2.35	2.62	2.25	2.72	1.34	1.36	6.74	6.42	6.20	1.44	1.25	1.23	4.60
Lu	0.31	0.26	0.36	0.41	0.33	0.42	0.21	0.19	1.06	1.03	0.97	0.22	0.19	0.20	0.69
Hf	1.92	1.07	1.84	1.94	1.63	2.01	4.46	5.60	11.80	9.07	8.63	4.13	4.22	5.94	3.50
Ta	0.08	0.14	0.20	0.21	0.32	0.40	0.36	0.50	0.70	0.79	0.77	2.55	0.54	0.86	0.80
Tl	0.04	0.05	0.07	0.08	0.05	0.04	0.05			0.38	0.29	0.26	0.41	0.43	
Pb	64.19	2.25	3.36	2.89	3.45	8.70	3.85	5.50	8.00	5.33	3.45	14.89	9.52	7.78	10.00
Bi	0.03	0.46	0.11	0.06	0.35	0.23	0.05	0.10	0.10	0.09	0.07	0.81	0.26	0.23	0.10
Th	0.11	0.02	0.10	0.11	0.15	0.20	6.17	2.90	3.50	3.74	4.13	24.06	6.19	10.38	4.90
U	0.12	0.02	0.03	0.04	0.10	0.08	1.11	1.80	1.10	0.80	0.87	3.47	1.41	2.41	1.30

[a] After Zhang et al. (2010).

Quartz in the BIF is generally thought to be the stable end product, which is the recrystallization product of initial amorphous silica precipitates during metamorphism (Mloszewska et al., 2012). Quartz can be found as inclusions within amphibole, suggesting that quartz was the early mineral phase before amphibole.

There are two-type garnets found in the BIF. For the lath-shaped garnet (II), it has an unusual origin, as denoted by its distinct crystal and minor ilmenite inclusions. It has been proposed that titanium in marine sediments originates from clastic input of terrigenous sources or hydrothermal solutions at an ocean ridge, based on the constancy of Al_2O_3/TiO_2 ratio and of REE patterns (Manikyamba et al., 1993). On the basis of the difference in chemical states of Ti in the Hamersley BIFs, Fukuda et al. (2001) suggested that Ti in magnetite may be precipitated from hydrothermal solutions at a Precambrian mid-oceanic ridge or hot-spot activity. On the other hand, Ti and Ti oxides in silicate phase originate from the weathering of terrigenous silicates exposed on land. Moreover, there are very simple mineral phases (grunerite and ilmenite) and straight grunerite lamella in the lath-shaped garnet fragments, which provide other supports to infer that the lath-shaped garnet was derived directly from early weathering of clastic detritus, not a product of polyphase metamorphism. However, for the near-equiaxed garnet grains (I), they may be a crystallization product of progressive metamorphism due to the reaction between original Al-rich clastics and silicate phases.

The most conspicuous mineral group in medium-grade metamorphosed BIF is that of Fe-rich amphiboles, such as grunerite, which can be produced in the reaction between quartz and Fe-rich carbonates, or the conversion from minnesotaite (Trendall and Morris, 1983; Klein, 2005). The Fe–Mg clinoamphiboles are

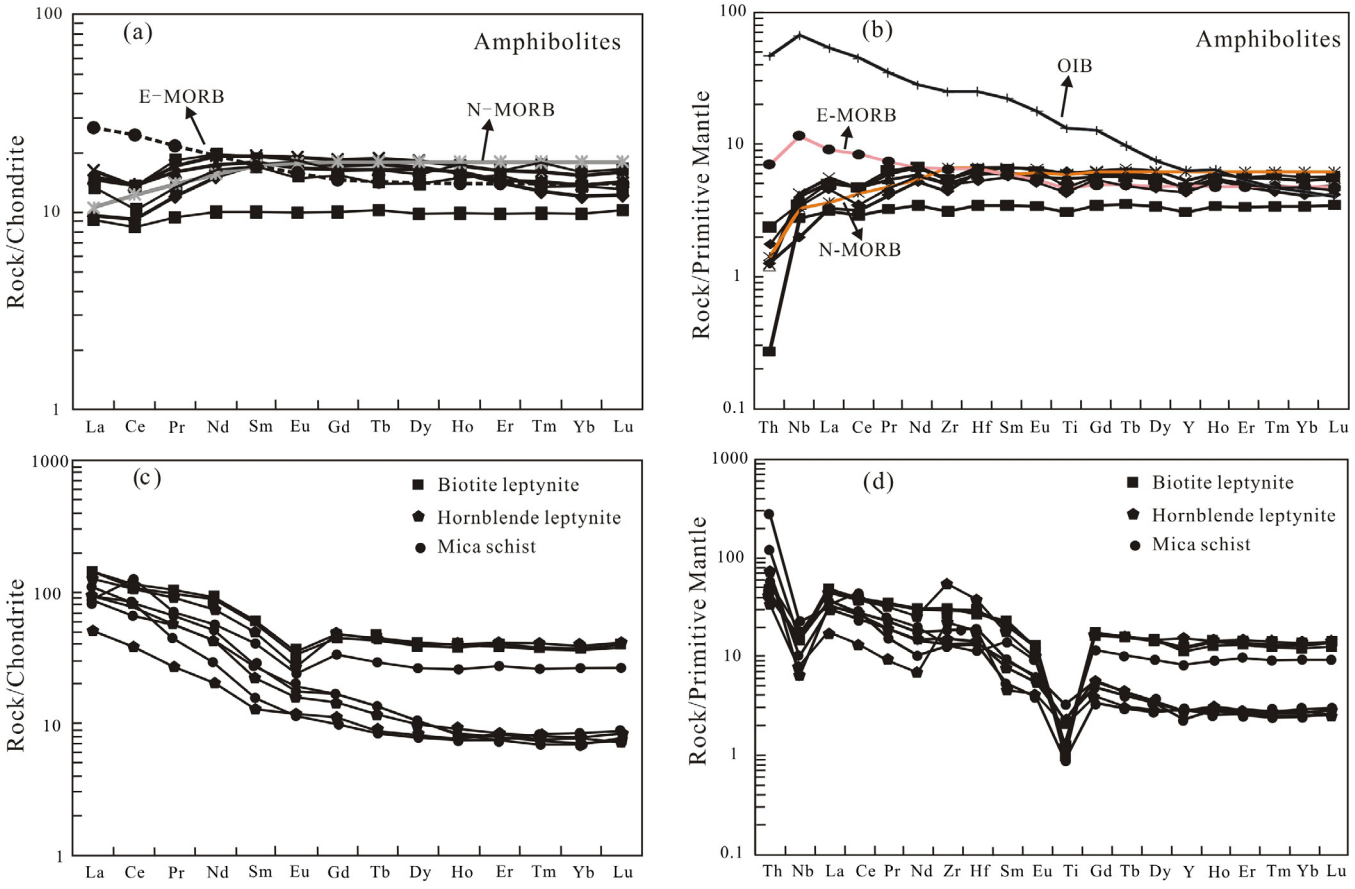

Fig. 12. Chondrite normalized REE, and primitive mantle normalized multielement diagrams. Normalizing values after Sun and McDonough (1989). (a) and (b) Amphibolites; (c) and (d) Leptynite and mica schist. Patterns for N-MORB, E-MORB, OIB (Sun and McDonough, 1989) are also shown for comparison.

commonly intergrown with Ca-clinoamphiboles such as actinolite (Klein, 1968). However, the ferro-actinolite in the BIF only occurs along the edge of grunerite, which is thought to be a consequence of metasomatism onto grunerite during the slow-cooling process from amphibolites-facies peak metamorphic temperature (Ross et al., 1969). The ferro-pargasite in the BIF has two distinct occurrences, likely representing two generations. The ferro-pargasite (I) associated with grunerite is likely to be formed through the reaction between Al-rich clastics and a Ca–Mg–Fe-bearing silicate precursor during metamorphism; whereas the other type (II), which is ubiquitous as moats surrounding garnet or growing along the cleavage, is considered to be a replacement mineral of garnet (I). This is possibly related to later fluid mobilization with external Na^+ and K^+ additives.

Calcite is often intergrown with grunerite, quartz and magnetite (Fig. 6f), presenting a fully equilibrated texture. A possible reaction between early Fe-rich carbonates (ferrodolomite) and quartz would have produced calcite during amphibolite facies metamorphic condition.

Taking the above into consideration, it can be concluded that magnetite, quartz, grunerite, garnet (I), ferro-pargasite (I) and calcite constitute an equilibrium assemblage under amphibolite facies metamorphism, whereas ferro-pargasite (II) and ferro-actinolite are replacement minerals related to fluid mobilization during retrogressive metamorphism.

6.2. Age and significance of the Wangjiazhuang BIF

The Wutai Group represents the majority of the WGB. Traditionally, the Wutai Group was subdivided into the lower, middle and upper sequences, which are the Shizui, Taihuai and Gaofan Subgroups, respectively (Fig. 2). The age of the Wutai Group was previously constrained by SHRIMP zircon dating of the meta-intermediate and felsic volcanic rocks at 2530–2515 Ma (Wilde et al., 2004, 2005). These zircon ages reveal no difference among volcanic rocks occupying different stratigraphic levels within the Wutai Group (seen from Fig. 2), which suggest that eruption of the volcanic rocks in these three subgroups are largely coeval. However, no reliable magmatic zircon ages are currently available for either the Jingangku Formation or mafic volcanic rocks. The Wangjiazhuang BIF occurring in the Jingangku Formation is interlayered with amphibolites, which have previously considered as metamorphosed basaltic rocks (Zhang et al., 2010). The combined results of CL images and U–Pb analyses provide robust evidence that the zircon grains from the metavolcanic layer were formed during a single magmatic event at ~2.54 Ga (Fig. 9). This age most likely represents the timing of mafic volcanism, which occurred synchronous with the deposition of the BIF. Considering that the zircon age predates the previous zircon ages of the intermediate and felsic volcanic rocks, we infer that the Wutai Group is a lithotectonic assemblage of volcanic-sedimentary rocks that formed in the period of 2543–2515 Ma. However, Wan et al. (2010) proposed that the Gaofan Subgroup is early Paleoproterozoic in age and is thus unrelated to the Wutai Group based on the detrital zircon ages of meta-sedimentary rocks. Therefore, the Gaofan Subgroup is likely to be disintegrated, and future detailed work is needed to confirm this.

The Fuping and Hengshan TTG gneisses are separated by the WGB. Recent SHRIMP and evaporation zircon dating on these two units indicates that they are almost coeval with the emplacement

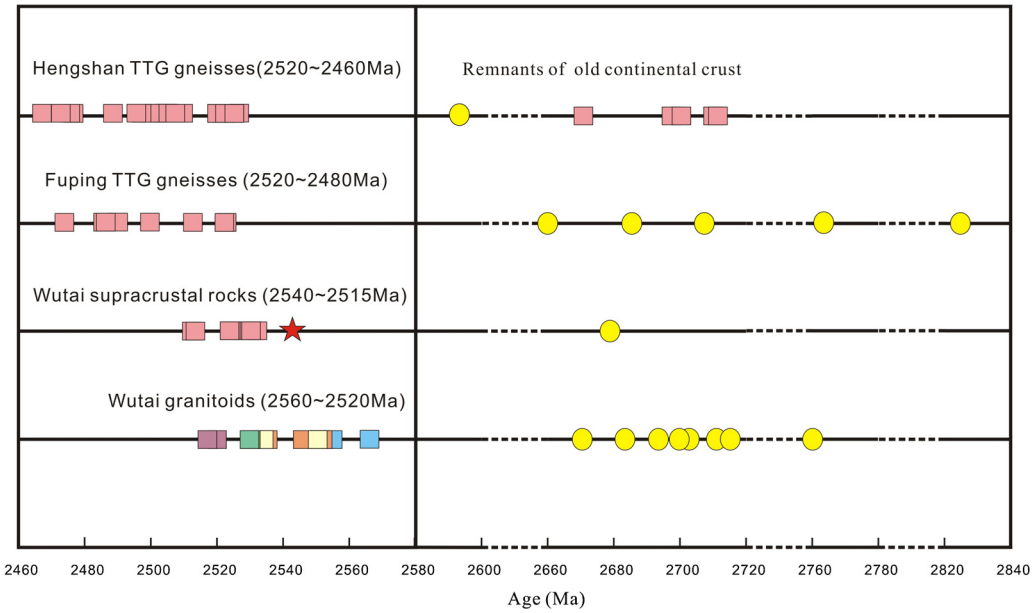

Fig. 13. Summary of age data of the Hengshan–Wutai–Fuping belt. Solid squares represent magmatic zircons; the red star represents the age of amphibolites in the Jingangku Formation; solid circles stand for inherited zircons. Data from Guan et al. (2002), Zhao et al. (2002), Kröner et al. (2005a,b), Zhao (2012), Wilde et al. (1997, 2004, 2005).

ages of the Fuping and Hengshan TTG gneisses between 2520 and 2480 Ma and 2520 and 2460 Ma, respectively (Guan et al., 2002; Zhao et al., 2002; Kröner et al., 2005a,b; Zhao, 2012) (Fig. 13). These data reveal that the Hengshan and Fuping TTG gneisses are slightly younger than the WGB, not supporting previous models that the Fuping and Hengshan complexes constitute an older basement below the WGB (Zhao et al., 2007). In addition, large amounts of granitoids are exposed in this area, such as the Ekou, Lanzhishan, Chechang-Beitai granites. SHRIMP zircon dating reveals that most of them intruded between 2560 and 2520 Ma (Wilde et al., 1997, 2005) (Fig. 13), which reflect the earliest arc-related magmatic event in the Hengshan–Wutai–Fuping belt.

The Wangjiazhuang BIF, similar to most of Algoma-type BIFs in the NCC, was formed in the Neoarchean (Wan et al., 2012a; Zhai and Santosh, 2013). In contrast with other BIF-bearing greenstone belts around the world (Table 6), the ages of BIFs occurring in the WGB are younger than that of other greenstone-type BIFs, which span from 3.8 to 2.5 Ga with the peak formation at 2.8–2.7 Ga. All greenstone-type BIFs in the NCC developed in the Neoarchean, which does not correspond with the peak crustal growth at 2.8–2.7 Ga in most cratons but is well consistent with intense tectonic-magmatic activity at ~2.5 Ga (Zhang et al., 2012b). These unique characteristics of greenstone belts in the NCC may suggest that significant systematic transformation of the NCC has been operating at ~2.5 Ga.

6.3. Source characteristics of the Wangjiazhuang BIF

6.3.1. Significant terrigenous input

Geochemical studies of BIFs have been used as a proxy to identify secular trends in Precambrian ocean chemistry. However, for BIFs that might have been affected by a number of processes including syn-depositional processes (clastic or volcanic contamination) and post-depositional processes (diagenesis, metamorphism, hydrothermal alteration, and weathering), geochemical characteristics of BIFs must be used with caution.

The Wangjiazhuang BIF samples contain high but variable concentrations of Al_2O_3 (>0.5%), HFSEs such as Zr, Sc and the transition metals. The high Al-content is reflected by the high modal content of garnet and ferro-pargasite in the BIF. In addition, there are positive correlations among Al_2O_3, TiO_2, HFSEs and REE (Fig. 14). These characteristics indicate significant terrigenous input into the BIF.

Possible syn-depositional contaminants of the iron formations include (1) volcanic ash, (2) sedimentary detritus and (3) material of uncertain origin such as phosphate grains (Thurston et al., 2012). The role of contaminants and phosphates can be estimated by use of the Th/U ratio. Phosphates, similar to other categories of contaminants, have Th/U ratios of ca. 3–5. When incorporated in the BIF, the ratio of Th/U can be raised. However, the Wangjiazhuang BIF samples display much more variable and mostly lower Th/U ratios of 0.79–6.52 and phosphate minerals including apatite and monazite were not observed in thin sections. In addition, they do not exhibit elevated Th/U with low Zr contents related to igneous debris (Fig. 14e), indicating little role for volcanic ash in the Wangjiazhuang BIF.

To further discriminate the source of contaminants between the volcanic ash and sedimentary detritus, binary plots of immobile element pairs can be used (McLennan et al., 1993). Available data from amphibolites, leptynite and mica schist are also plotted in Fig. 14a and b. The BIF samples plot close to leptynite and mica schist, suggesting that detrital and felsic volcanic sources contributed to the contaminants. Moreover, Bau and Alexander (2009) studied the Zr–Hf–Ta systematics in detail in BIFs and found that the Zr/Hf ratios of clastic sediments cluster around the chondritic Zr/Hf ratio and that of the upper continental crust. In Fig. 14f, Zr/Hf ratios of the Wangjiazhuang BIF samples plot close to the chondritic and upper crustal ratios and away from the ratios of N-MORB, indicating contaminants in the BIF were mainly derived from sedimentary detritus.

Terrigenous input represents a significant continental source of dissolved Fe (II) as a fraction of the total Fe of the Wangjiazhuang BIF. The net flux of iron to the oceans via river run-off is severely limited under oxygenic conditions (Chester, 2000), but before the great oxygenation event (2.45–2.2 Ga), prevailing anoxic weathering existed, which would have facilitated the mobilization of Fe(II) and its transport to the ocean (Lascelles, 2007). In addition, the loss of Fe in pre-2.2 Ga paleosols provides another support to this conclusion (Rye and Holland, 2000). However, we cannot

Table 6
Summary of ages and geodynamic settings for BIF-bearing Archean greenstone terranes, updated from Angerer et al. (2013). Reference: (1) Polat et al. (2002), (2) Parman et al. (2001), (3) Angerer et al. (2013), (4) Puchtel (2004), (5) Wyman and Kerrich (2012), (6) Kerrich et al. (1999), (7) Jelsma et al. (1996), (8) Shimizu et al. (2005), (9) Kerrich et al. (1998), (10) Srivastava et al. (2004), (11) Wang et al. (2004), (12) Ma et al. (2013), (13) Zhai and Santosh (2013), (14) Wan et al. (2012b), (15) W. Wang et al. (2013).

Craton	Terrane/greenstone belt	Aga (Ga)	Inferred geodynamic setting	Reference
Greenland	Isua	3.8	Convergent Margin Suprasubduction Zone	1
Kaapvaal	Barberton	3.5	Convergent Margin Suprasubduction Zone	2
Yilgarn	Youanmi (Southern Cross)	3	Plume-arc interaction	3
Siberian	Olondo	3	Convergent Margin Suprasubduction Zone	4
Yilgarn	Youanmi (Murchison)	2.8	Plume-arc interaction	5
Superior	Pickle Lake	2.8	Plume-arc interaction	6
Zimbabwe	Belingwean	2.7	Convergent Margin Suprasubduction Zone or Intracontinental rifting related to mantle plume	7,8
Superior	Abitibi	2.7	Plume-arc interaction	9
Singhbhum	Bastar	2.7	Convergent Margin Suprasubduction Zone	10
North China	Wutai	2.5	Convergent Margin Suprasubduction Zone	11 and this study
	Guyang	2.5	Convergent Margin Suprasubduction Zone	12
	Hongtoushan	2.5	Convergent Margin Suprasubduction Zone	13
	Western Shandong Province	2.7~2.5	Convergent Margin Suprasubduction Zone	14,15

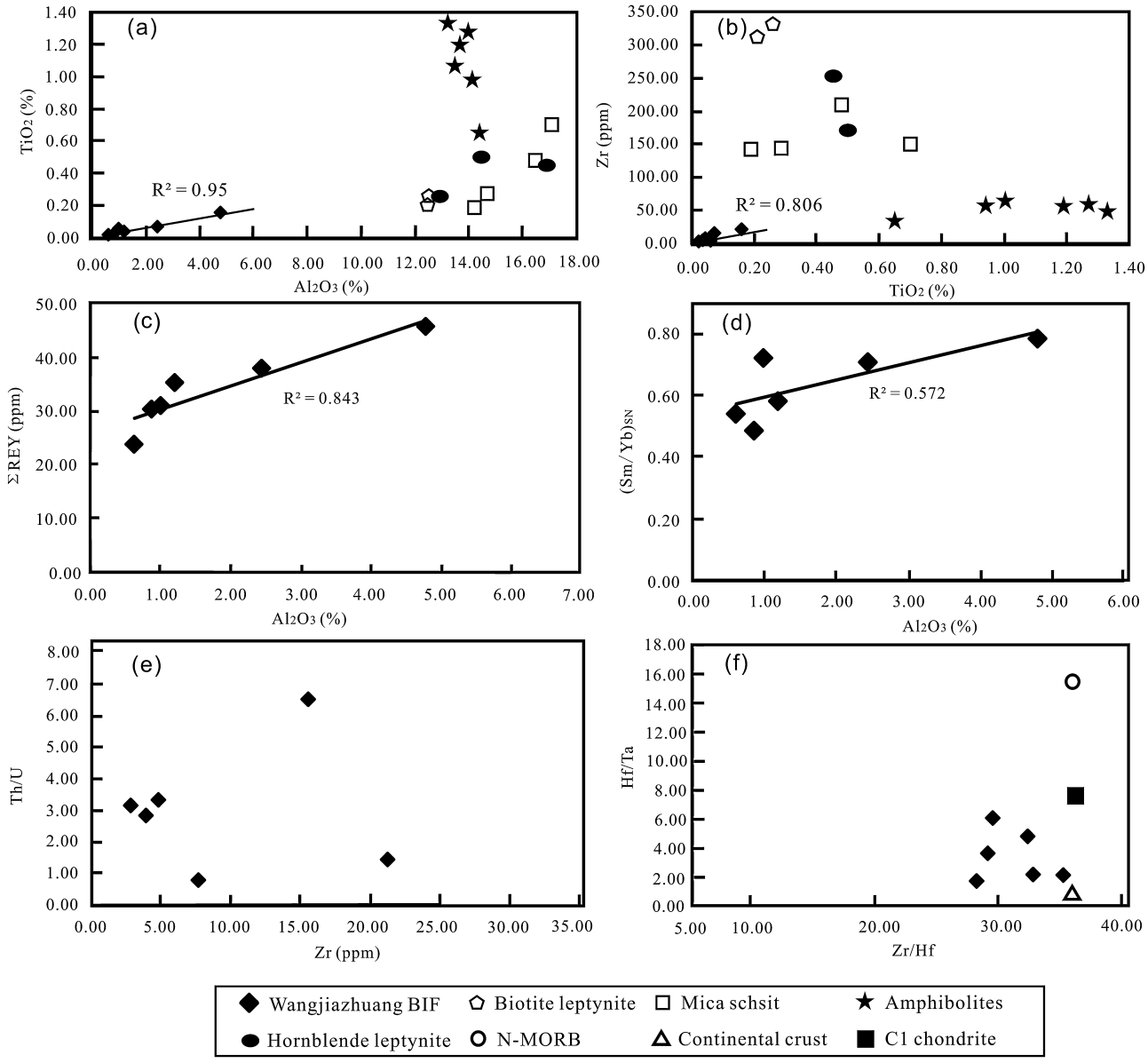

Fig. 14. Correlation diagrams showing the extent of contamination. (a) Al_2O_3 vs. TiO_2 for the Wangjiazhuang BIF and associated lithologies; (b) TiO_2 vs. Zr for the Wangjiazhuang BIF and associated lithologies; (c) Al_2O_3 vs. ΣREE for the Wangjiazhuang BIF; (d) Al_2O_3 vs. $(Sm/Yb)_{SN}$ for the Wangjiazhuang BIF. Note the positive correlation between different immobile elements in the Wangjiazhuang BIF; (e) Zr vs. Th/U for the Wangjiazhuang BIF; (f) Zr/Hf vs. Hf/Ta for the Wangjiazhuang BIF, average continental crust (data from Rudnick and Gao, 2003), C1 chondrite and N-MORB (data from Sun and McDonough, 1989).

quantify amounts of iron only based on the high concentrations of lithogenous elements (e.g., Al_2O_3 and Zr).

6.3.2. Significant seawater input

The REY in BIFs are generally regarded as being immobile during most geological processes (Bingen et al., 1996), and the effects of metamorphism on the REE distribution in iron formations have been found to be only of minor importance in most cases (Bau and Dulski, 1996). Minor amounts of clastic materials, when incorporated into BIFs during depositional processes, are sufficient to result in decreases in Eu/Sm, and Y/Ho ratios and an increase in Sm/Yb ratios (Bau, 1993). The Wangjiazhuang BIF samples have higher REY abundances than other BIFs such as the Isua BIF (Bolhar et al., 2004), which is attributed to different degrees of terrigenous contamination (Fig. 10). Even so, the Wangjiazhuang BIF samples display positive La anomalies, a relative depletion of LREE and MREE compared with HREE, superchondritic Y/Ho ratios (>26), which are typical features of modern seawater. Y/Ho ratios (average of 29) of the BIF fall between those of hydrothermal fluids and terrestrial materials (~26) and modern seawater (>44), and are much lower than other typical BIFs (including the Shuichang BIF in China (average of 41) (Zhang et al., 2011), the Isua BIF (average of 42) (Bolhar et al., 2004), and the Dales Gorge BIF (average of 43) (Pecoits et al., 2009)). These may suggest that the Y/Ho ratio in the seawater was suppressed by hydrothermal fluids and/or crustal detritus. The positive Y anomalies (1.10–1.26) in the BIF are distinct from slowly growing modern marine hydrogenetic ferromanganese with negative Y anomalies but similar to rapidly precipitated modern marine hydrothermal ferromanganese precipitates. It can be inferred that the IF precipitation occurred very rapidly and the scavenged REY could not be in exchange equilibrium with ambient seawater (Bau and Dulski, 1996). In addition, other BIFs of upper Wenxi and Bozhiyan Formations in the Wutai Group (Li et al., 2010b) display identical REY patterns with the Wangjiazhuang BIF. Thus, the Wangjiazhuang BIF can well constrain total characteristics of BIFs in the WGB.

The Wangjiazhuang BIF samples display positive Eu anomalies (average of 2.39) typical of Archean BIFs, indicating some high-T (>350 °C) hydrothermal fluids input. Frei et al. (2008) found that $(Eu/Eu^*)_{SN}$ ratios of Precambrian IFs decrease with the decrease of their age, which they interpret as a consequence of the diminishing thermal and hydrothermal activities with decreasing age (Condie, 1997; Arndt et al., 2008). However, combining with $(Eu/Eu^*)_{SN}$ ratios of some BIFs, for example, the 3.7 Ga Isua BIF (average of 2.92) (Bolhar et al., 2004); the 2.9 Ga Itilliarsuk BIF (average of 1.63) (Haugaard et al., 2013); the 2.2 Ga Yuanjiacun BIF (average of 2.36) (Wang et al., 2014), Eu anomalies in the Wangjiazhuang BIF are less marked than the Isua BIF, but similar to the other two BIFs, which could not support the previous deduction. Large positive Eu anomalies observed in the BIFs possessing seawater-like REY distributions indicate a significant high-T hydrothermal fluid input to ancient oceans. Unfortunately, positive Eu anomalies cannot be used for mass fraction calculations regarding the mixing of high-T hydrothermal fluids and ambient seawater, but rather reflect only the temperature of the hydrothermal system (Bau and Möller, 1993; Alexander et al., 2008). In addition, the observed small-scale variation of Eu anomalies among the BIF samples may indicate short-term variability of $(Eu/Eu^*)_{SN}$ ratios of seawater, most likely resulting from temporal variation of the activity of high-T fluids rather than post-depositional metamorphism (Bau and Dulski, 1996; Wang et al., 2014).

From above it can be concluded that three decoupled sources control the materials of the BIF: high-T hydrothermal fluids, seawater and terrigenous input. Considering that REY patterns of terrigenous input are difficult to characterize, a conservative two-component mixing model between high-T hydrothermal fluids and modern seawater is used to assess a high-T hydrothermal fluid contribution (Alexander et al., 2008). In Fig. 15, Sm/Yb ratios are used to define the range of hydrothermal fluids and seawater combining with Y/Ho ratios. Similar to other BIFs such as the Isua BIF, a small proportion of high-temperature hydrothermal fluids (<1%) is adequate for producing the Y/Ho and Sm/Yb ratios observed within the Wangjiazhuang BIF. In addition, because of terrigenous input as an additional REY source, which would have resulted in a decrease of Y/Ho ratios and an increase of Sm/Yb ratios, a high-T hydrothermal fluid contribution would be amplified. Thus, Y/Ho and Sm/Yb ratios must be adjusted along the direction of a red arrow to achieve a comparatively authentic mixing model (Fig. 15). The Wangjiazhuang BIF samples would plot closer to the seawater range. Therefore, it appears that a relatively lesser high-T

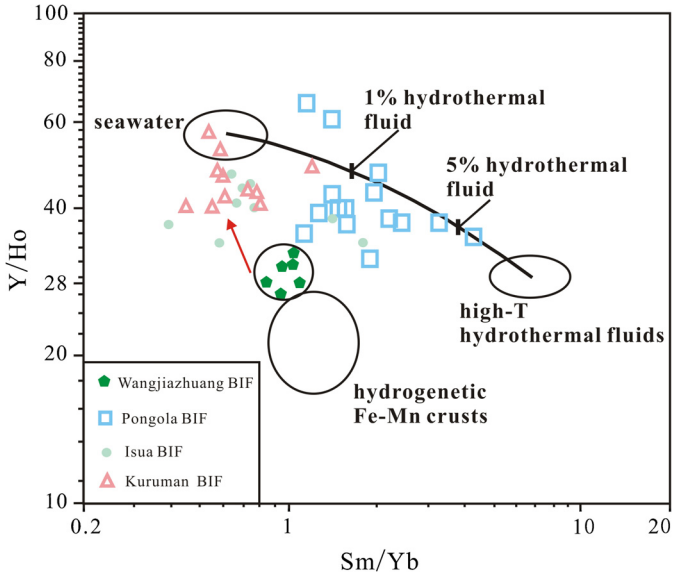

Fig. 15. Two-component conservative mixing lines of Sm/Yb vs. Y/Ho ratios (after Alexander et al., 2008) for the Wangjiazhuang BIF, Isua BIF (Bolhar et al., 2004), Kuruman BIF (Bau and Dulski, 1996), Pongola BIF (Alexander et al., 2008), high-T (>350 °C) hydrothermal fluids (Bau and Dulski, 1999), Pacific seawater (Alibo and Nozaki, 1999), and hydrogenetic Fe–Mn crusts.

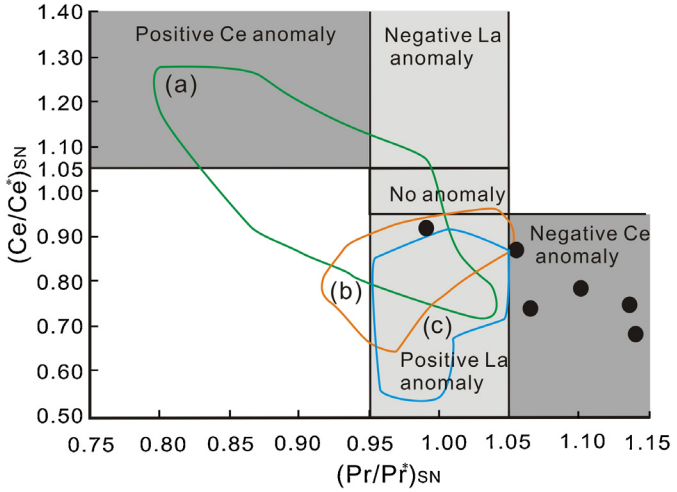

Fig. 16. Plot of Ce and Pr anomalies normalized to PAAS for the Wangjiazhuang BIF to discriminate between positive La and true Ce anomalies (Bau and Dulski, 1996). Plots of foreign late Paleoproterozoic (<2.0 Ga) (field a) and Archean and early Paleoproterozoic (>2.4 Ga) (field b) iron formations, Chinese Archean (>2.5 Ga) (field c) iron formations are also included.

Data from Li et al. (2008), Planavsky et al. (2010), Zhang et al. (2011).

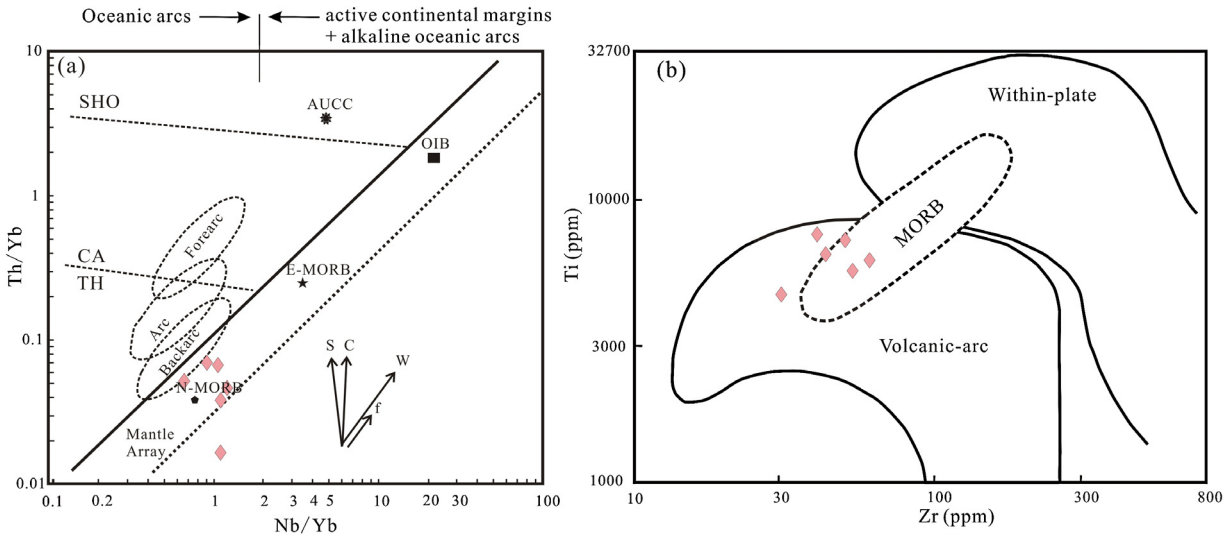

Fig. 17. Plots of (a) Th/Yb vs. Nb/Yb and (b) Zr vs. Ti for amphibolites. The mantle array includes constructive plate boundary magmas (N-MORB: normal mid-ocean ridge basalts; E-MORB: enriched mid ocean ridge basalts) and within-plate alkaline basalts (ocean island basalts; OIB). AUCC is Archean upper continental crust. Fields for convergent margin basalts include the tholeiitic (TH), calc-alkaline (CA), and shoshonitic (SHO) magma series. The vectors S, C, W, and f refer to subduction zone component, crustal contamination, within plate fractionation, and fractional crystallization respectively (after Pearce, 2008; Angerer et al., 2013). Forearc, arc, and back-arc fields are of recent convergent margins (Metcalf and Shervais, 2008).

hydrothermal fluid contribution may account for REY patterns in the BIF.

6.3.3. Redox state of ancient seawater

The capture and preservation of aqueous REE patterns in the BIFs provides a window into ancient ocean chemistry and redox state. Ce anomalies of the BIFs as a potential tool can be used to constrain redox state of seawater. However, the discrimination and identification of Ce anomalies is complicated by possibly anomalous abundances of La. Bau and Dulski (1996) established a discrimination diagram, based upon combined $(Ce/Ce^*)_{SN}$ and $(Pr/Pr^*)_{SN}$ values, to distinguish "real" from apparent anomalies of Ce in the BIFs. In Fig. 16, plots for late Paleoproterozoic (2.0–1.8 Ga) and Archean and early Paleoproterozoic (>2.4 Ga) iron formations (Li et al., 2008; Planavsky et al., 2010; Zhang et al., 2011) around the world are also shown. Most of the Wangjiazhuang BIF samples display significant negative Ce anomalies, which are not typically encountered in the Archean and Paleoproterozoic BIFs. In general, modern oxygenated marine water shows a strong negative Ce anomaly when REE data are normalized to shale compositions. Given dissolved oxygen, Ce (III) in marine water is oxidized and sequestered as CeO_2 or $Ce(OH)_4$ largely by Mn-hydroxides and oxyhydroxides (Elderfield et al., 1981), resulting in variable large positive Ce anomalies in Recent and Cenozoic Mn-nodules and crusts and complementary negative anomalies in oxygenated seawater. The appearance of true negative Ce anomalies in the Wangjiazhuang BIF, similar to that in some early Paleoproterozoic BIFs from the Black Hills (Frei et al., 2008), can infer the oxygenation of bottom waters.

In addition, it is also possible to utilize Th-U decoupling to qualitatively constrain oxygen levels in the Neoarchean surface system (Bau and Alexander, 2009). The Th/U ratio in epiclastic sedimentary rocks is not very variable and falls close to the Th/U ratio (~3.9) of average upper continental crust (Condie, 1993). Decoupling of Th and U is commonly attributed to oxidation of immobile U^{4+} to mobile U^{6+} during oxic weathering or diagenesis, eventually resulting in a lower seawater Th/U ratio (Collerson and Kamber, 1999). The fractionated Th/U ratios (0.79–6.52) observed in the Wangjiazhuang BIF suggest ambient seawater had received preferential U input, indicating mildly oxidizing conditions in the source area of U. This is in accordance with the appearance of negative Ce anomalies in the Wangjiazhuang BIF.

The Wangjiazhuang BIF is a typical Archean greenstone-type BIF with a small scale. Barley et al. (1998) related Archean BIF deposition to the interplay among tectonics, magmatism, and eustacy. Algoma-type BIFs were regarded to reflect intrabasinal pulses of magmatic and hydrothermal activity during the deposition of volcano-sedimentary greenstone successions (Bekker et al., 2010). Thus, the geochemistry of the Wangjiazhuang BIF may reflect local volcanic or hydrothermal conditions in restricted marine basins and therefore provides no information about the redox state of the global ocean. Therefore, these distinctive geochemical characteristics of the Wangjiazhuang BIF imply that oxidative processes were operating at the Neoarchean/Paleoproterozoic boundary, at least in restricted basins, which permitted Ce (III) oxidation and formation of Fe (III) oxyhydroxides.

6.4. Tectonic setting of the Wangjiazhuang BIF

The trace element characteristics of lithologies associated with the Wangjiazhuang BIF, including amphibolites and leptynites, are all consistent with a subduction zone geochemical signature (Pearce and Peate, 1995). In particular, the geochemistry of amphibolite samples displays a striking similarity with that of N-MORB and BABB. Collectively, these features likely reflect an interaction between depleted mantle-derive (MORB-like) and subduction zone-derived melts or fluids. On the Th/Yb versus Nb/Yb and Zr versus Ti discrimination plots (Fig. 17) (Pearce, 1982, 2008), amphibolite samples plot close to or in the field of N-MORB and volcanic-arc basalts, also indicating their geochemical affinity with both MORB- and arc-like components. Thus, a back-arc basin setting is the possible tectonic setting of the BIF.

In addition, previous geochemical research on volcanic rocks in the WGB can also provide some other evidence. Bai et al. (1992) revealed that the majority of amphibolites and greenschists in the Wutai Group have an affinity with calc-alkaline basalts or arc tholeiites. Wang et al. (2004) recognized a MORB-arc basalt-adakite association in the WGB and identified the proposed mixing of MORB-type magmas and subduction-related magmas based on the geochemistry of volcanics. Then, Polat et al. (2005) conducted

the same study on this suit of volcanics and also confirmed this special interaction. However, they suggested that such interaction took place in a forearc rather than in a back-arc geodynamic setting and was associated with a ridge subduction. It is widely accepted that boninite and high-Mg andesite are typical lithologies developed in a fore-arc basin setting (Shuto et al., 2006; Rolland et al., 2009). Nevertheless, there are few reports about the identification of this typical association in the WGB.

As seen in Table 6, nearly all of Archean BIF-bearing greenstone belt terranes worldwide are formed in a convergent margin suprasubduction zone. In addition, plume-arc interactions are also responsible for formation of some greenstone belts, such as the Abitibi and Pickle Lake greenstone belts. In China, typical greenstone-type BIFs, for example, the Wutai, Guyang and Hongtoushan greenstone belts, have similar ages (~2.5 Ga) and inferred geodynamic settings (arc/back-arc basins) with that of most BIFs in the NCC (Zhang et al., 2012b).

7. Conclusion

The Wangjiazhuang BIF is one of representative BIFs in the Jingangku Formaiton of the Wutai Group. Based on SIMS zircon U–Pb analyses of the meta-basalt interbeds, they were formed at 2.54 Ga, representing the formation age of the BIF.

The precursors of the BIF are composed of ferric-oxyhydroxides, carbonate oozes, silicate phases rich in Al–Ca–Mg–Fe and amorphous silica. There is a significant clastic component, which was mainly derived from sedimentary detritus attributed to continental weathering. REE+Y patterns are typical of ambient seawater, and they are imprinted by high-T (>350 °C) hydrothermal fluid, characterized by consistently positive Eu anomalies. Significantly, most of the BIF samples display true negative Ce anomalies despite metamorphic overprint, which are not common in the Archean and Paleoproterozoic BIFs. This may imply that oxidative processes have operated at the Neoarchean/Paleoproterozoic boundary, at least in restricted basins, not reflecting the redox state of the global ocean.

Trace element and REE characteristics of amphibolites likely reflect an interaction between depleted mantle-derive (MORB-like) and subduction zone-derived melts or fluids, suggesting that they erupted in the back-arc basin. However, further available data are needed to determine whether the Wutai arc was an oceanic island arc or a continental margin magmatic arc.

Acknowledgements

This work was supported by the Major State Basic Research Programme of the People's Republic of China (No. 2012CB416601) and the Knowledge Innovation Programme of the Chinese Academy of Sciences (No. KZCX2-YW-Q04-07). Much thanks for Xiaojing Zhang, Huaying Wu, they give us help in SIMS analyses and field work. We also thank Yusheng Wan, Peng Peng, Allen P. Nutman and an anonymous reviewer for their constructive comments.

References

Alexander, B.W., Bau, M., Andersson, P., Dulski, P., 2008. Continentally-derived solutes in shallow Archean seawater: rare earth element and Nd isotope evidence in iron formation from the 2.9 Ga Pongola Supergroup, South Africa. Geochim. Cosmochim. Acta 72, 378–394.

Alibo, D.S., Nozaki, Y., 1999. Rare earth elements in seawater: particle association, shale-normalization, and Ce oxidation. Geochim. Cosmochim. Acta 63, 363–372.

Angerer, A., Kerrich, R., Hagemann, S.G., 2013. Geochemistry of a komatiitic, boninitic, and tholeiitic basalt association in the Mesoarchean Koolyanobbing greenstone belt, Southern Cross Domain, Yilgarn Craton: implications for mantle sources and geodynamic setting of banded iron formation. Precambrian Res. 224, 110–128.

Arndt, N.T., Barnes, S.J., Lesher, C.M., 2008. Komatiite. Cambridge University Press, Cambridge, pp. 488 pp.

Ayres, D.E., 1972. Genesis of iron-bearing minerals in banded iron formation mesobands in the Dales Gorge Member, Hamersley Group, Western Australia. Econ. Geol. 67, 1214–1233.

Bai, J., 1986. The Early Precambrian Geology of Wutaishan. Tianjin Science and Technology Press, Tianjin, China, pp. 435 pp.

Bai, J., Wang, R.Z., Guo, J.J., 1992. The Major Geologic Events of Early Precambrian and Their Dating in Wutaishan Region. Geological Publishing House, Beijing, pp. 34–55 (in Chinese).

Barley, M.E., Kerrich, R., Krapež, B., Groves, D.I., 1998. The 2.72–2.60 Ga bonanza: metallogenic and environmental consequences of the interaction between mantle plumes, lithospheric tectonics and global cyclicity. Precambrian Res. 91, 65–90.

Bau, M., 1993. Effects of syn- and post-depositional processes on the rare-earth element distribution in Precambrian Iron-formations. Eur. J. Mineral. 5, 257–267.

Bau, M., Alexander, B.W., 2009. Distribution of high field strength elements (Y, Zr, REE, Hf, Ta, Th, U) in adjacent magnetite and chert bands and in reference standards FeR-3 and FeR-4 from the Temagami iron-formation, Canada, and the redox level of the Neoarchean ocean. Precambrian Res. 174, 337–346.

Bau, M., Dulski, P., 1996. Distribution of yttrium and rare-earth elements in the Penge and Kuruman iron-formations, Transvaal Supergroup, South Africa. Precambrian Res. 79, 37–55.

Bau, M., Dulski, P., 1999. Comparing yttrium and rare-earth in hydrothermal fluids from the mid-Atlantic ridge: implications for Y and REE behaviour during near vent mixing and for the Y/Ho ratio of Proterozoic seawater. Chem. Geol. 155, 77–90.

Bau, M., Möller, P., 1993. Rare earth element systematics of the chemically precipitated component in early Precambrian iron formations and the evolution of the terrestrial atmosphere–hydrosphere–lithosphere system. Geochim. Cosmochim. Acta 57, 2239–2249.

Bekker, A., Slack, J.F., Planavsky, N., Krapež, B., Hofmann, A., Konhauser, K.O., Rouxel, O.J., 2010. Iron formation: the sedimentary product of a complex interplay among mantle, tectonic oceanic, and biospheric processes. Econ. Geol. 105, 467–508.

Bingen, B., Demaiffe, D., Hergoten, J., 1996. Redistribution of REE, thorium and uranium over accessory minerals in the course of amphibolite to granulite facies metamorphism: the role of apatite and monazite in orthogneisses from southeastern Norway. Geochim. Cosmochim. Acta 60, 1341–1354.

Bolhar, R., Kamber, B.S., Moorbath, S., Fedo, C.M., Whitehouse, M.J., 2004. Characterisation of early Archaean chemical sediments by trace element signatures. Earth Planet. Sci. Lett. 222, 43–60.

Bolhar, R., Van Kranendonk, M.J., 2007. A non-marine depositional setting for the northern Fortescue Group Pilbara Craton, inferred from trace element geochemistry of stromatolitic carbonates. Precambrian Res. 155, 229–250.

Chester, R., 2000. Marine Geochemistry, second ed. Blackwell Science, Oxford.

Collerson, K.D., Kamber, B.S., 1999. Evolution of the continents and the atmosphere inferred from Th–U–Nb systematics of the depleted mantle. Science 283, 1519–1522.

Condie, K.C., 1993. Chemical composition and evolution of the upper continental crust: contrasting results from surface samples and shales. Chem. Geol. 104, 1–37.

Condie, K.C., 1997. Plate Tectonics and Crustal Evolution. Butterworth-Heinemann, Oxford, pp. 282 pp.

Dai, Y.P., Zhang, L.C., Wang, C.L., Liu, L., Cui, M.L., Zhu, M.T., Xiang, P., 2012. Genetic type, formation age and tectonic setting of the Waitoushan banded iron formation Benxi, Liaoning Province. Acta Petrol. Sin. 28, 3574–3594.

Deer, W., Howie, R., Zussman, J., 1992. The Rock Forming Minerals. Longman Scientific and Technical, Harlow, UK, pp. p696.

Elderfield, H., Hawkesworth, C.J., Greaves, M.J., Calvert, S.E., 1981. Rare earth element geochemistry of oceanic ferromanganese nodules and associated sediments. Geochim. Cosmochim. Acta 45, 513–528.

Frei, R., Dahl, P.S., Duke, E.F., Frei, K.M., Hansen, T.R., Frandsson, M.M., Jensen, L.A., 2008. Trace element and isotopic characterization of Neoarchean and Paleoproterozoic iron formations in the Black Hills (South Dakota USA): assessment of chemical change during 2.9–1.9 Ga deposition bracketing the 2.4–2.2 Ga first rise of atmospheric oxygen. Precambrian Res. 162, 441–474.

Fukuda, K., Matsunaga, M., Kato, Y., Nakai, I., 2001. Chemical speciation of trace titanium in Hamersley banded iron formations by X-ray fluorescence imaging and xanes analysis. J. Trace Microprobe Tech. 19, 509–519.

Geng, Y.S., Wan, Y.S., Yang, C.H., 2008. The Set of Main Geological Events in the Paleoproterozoic Lüliang Area, Shanxi Province, Beijing. Geological Publishing House, Beijing, pp. 515–533 (in Chinese).

Ghazi, J.M., Moazzen, M., Rahgoshay, M., Moghadam, H.S., 2012. Geochemical characteristics of basaltic rocks from the Nain ophiolite (Central Iran); constraints on mantle wedge source evolution in an oceanic back arc basin and a geodynamical model. Tectonophysics 574, 92–104.

González, P.D., Sato, A.M., Llambías, E.J., Petronilho, L.A., 2009. Petrology and geochemistry of the banded iron formation in the Eastern Sierras Pampeanas of San Luis (Argentina): implications for the evolution of the Nogolí Metamorphic Complex. J. S. Am. Earth Sci. 28, 89–112.

Gross, G.A., 1980. A classification of iron formations based on depositional environments. Can. Mineral. 18, 215–222.

Gross, G.A., 1996. Algoma-type previous term iron-formation. Next term. In: Lefebure, D., Höy, T. (Eds.), Selected British Columbia Mineral Deposits Profiles 2. Ottawa British Columbia Ministry of Employment and Investment Open File, pp. 25–28.

Guan, H., Sun, M., Wilde, S.A., Zhou, X.H., Zhai, M.G., 2002. SHRIMP U–Pb zircon geochronology of the Fuping complex: implications for formation and assembly of the North China Craton. Precambrian Res. 113, 1–18.
Hamade, T., Konhauser, K.O., Raiswell, R., Goldsmith, S., Morris, R.C., 2003. Using Ge/Si ratio to decouple iron and silica fluxes in Precambrian banded iron formations. Geology 31, 35–38.
Haugaard, R., Frei, R., Stendal, H., Konhauser, K.O., 2013. Petrology and geochemistry of the ~2.9 Ga Itilliarsuk banded iron formation and associated supracrustal rocks, West Greenland: Source characteristics and depositional environment. Precambrian Res. 229, 150–176.
Henderson, P., 1984. General geochemical properties and abundances of the rare earth elements. In: Henderson, P. (Ed.), Rare Earth Element Geochemistry, vol. 2. Developments in Geochemistry, Amsterdam, Elsevier, pp. 1–32.
Isley, A.E., 1995. Hydrothermal plumes and the delivery of iron to banded iron formation. J. Geol. 103, 169–185.
James, H.L., 1954. Sedimentary facies of iron-formation. Econ. Geol. 49, 235–293.
Jelsma, H.A., Vinyu, M.L., Valbracht, P.J., Davies, G.R., Wijbrans, J.R., Verdurmen, A.T., 1996. Constraints on Archean crustal evolution of the Zimbabwe Craton: a U–Pb zircon Sm–Nd and Pb–Pb whole-rock isotope study. Contrib. Mineral. Petrol. 124, 55–70.
Kato, Y., Ohta, I., Tsunematsu, T., Watanabe, Y., Isozaki, Y., Maruyama, S., Imai, N., 1998. Rare earth element variations in mid-Archean banded iron formations: implications for the chemistry of ocean and plate tectonics. Geochim. Cosmochim. Acta 62, 3475–3497.
Kerrich, R., Wyman, D., Fan, J., Bleeker, W., 1998. Boninite series: low Ti-tholeiite associations from the 2.7 Ga Abitibi greenstone belt. Earth Planet. Sci. Lett. 164, 303–316.
Kerrich, R., Polat, A., Wyman, D., Hollings, P., 1999. Trace element systematics of Mg-, to Fe-tholeiitic basalt suites of the Superior Province: implications for Archean mantle reservoirs and greenstone belt genesis. Lithos 46, 163–187.
Klein, C., 1968. Coexisting amphiboles. J. Petrol. 9, 281–330.
Klein, C., 2005. Some Precambrian banded iron-formations (BIFs) from around the world: their age, geologic setting, mineralogy, metamorphism, geochemistry, and origins. Am. Mineral. 90, 1473–1499.
Kröner, A., Wilde, S.A., Li, J.H., Wang, K.Y., 2005a. Age and evolution of a late Archaean to early Palaeozoic upper to lower crustal section in the Wutaishan/Hengshan/Fuping terrain of northern China. J. Asian Earth Sci. 24, 577–595.
Kröner, A., Wilde, S.A., O'Brien, P.J., Li, J.H., Passchier, C.W., Walte, N.P., Liu, D.Y., 2005b. Field relationships, geochemistry, zircon ages and evolution of a Neoarchaean to Palaeoproterozoic lower crustal section in the Hengshan Terrain of Northern China. Acta Geol. Sin. 79, 605–629.
Kröner, A., Wilde, S.A., Zhao, G.C., O'Brien, P.J., Sun, M., Liu, D.Y., Wan, Y.S., Liu, S.W., Guo, J.H., 2006. Zircon geochronology and metamorphic evolution of mafic dykes in the Hengshan Complex of northern China: evidence for late Palaeoproterozoic extension and subsequent high-pressure metamorphism in the North China Craton. Precambrian Res. 146, 45–67.
Kusky, T.M., Li, J.H., 2003. Paleoproterozoic tectonic evolution of the North China Craton. J. Asian Earth Sci. 22, 383–397.
Lascelles, D.F., 2007. Black smokers and density currents: a uniformitarian model for the genesis of banded iron-formations. Ore Geol. Rev. 32, 381–411.
Li, J.H., Kusky, T., Niu, X.L., Jun, F., Polat, A., 2004. Neoarchean massive sulfide of Wutai Mountain, north China: a black smoker chimney and mound complex within 2.50 Ga-old oceanic crush. In: Kusky, T. (Ed.), Precambrian Ophiolites and Related Rocks. Developments in Precambrian Geology. Elsevier, Amsterdam, pp. 339–362.
Li, X.H., Liu, Y., Li, Q.L., Guo, C.H., Chamberlain, K.R., 2009. Precise determination of Phanerozoic zircon Pb/Pb age by multi-collector SIMS without external standardization. Geochem. Geophys. Geosyst. 10, Q04010.
Li, Y.H., (Master thesis) 2008. The study on geological features and genesis of iron deposit in Wangjiazhuang Region, Yuanping City, Shanxi Province. China University of Geosciences, Beijing, pp. 48 pp.
Li, Y.H., Hou, K.J., Wan, D.F., Zhang, Z.J., Yue, G.L., 2010a. Formation mechanism of Precambrian banded iron formation and atmosphere and ocean during early stage of the earth. Acta Geol. Sin. 80, 1359–1373.
Li, Z.H., Zhu, X.K., Tang, S.H., 2008. Characters of Fe isotopes and rare earth elements of banded iron formations from Anshan-Benxi area: implications for Fe source. Acta Petrol. Mineral. 27, 285–290.
Li, Z.H., Zhu, X.K., Tang, S.H., Li, J., Liu, H., 2010b. Characteristics of rare earth elements and geological significations of BIFs from Jidong, Wutai and Lüliang area. Geoscience 24, 840–846.
Liu, S.W., Zhang, J., Li, Q.G., Zhang, L.F., Wang, W., Yang, P.T., 2012. Geochemistry and U–Pb zircon ages of metamorphic volcanic rocks of the Paleoproterozoic Lüliang Complex and constraints on the evolution of the Trans-North China Orogen, Wutai and Lüliang area. Precambrian Res. 222, 173–190.
Ludwig, K., 2001. Isoplot/Ex, rev 2. 49. A Geochronological Toolkit for Microsoft Excel. Berkeley Geochronology Center, Special Publications, 1a.
Luo, H., Chen, Z.H., Shen, B.F., 1999. The mineralized age of Archean BIF-hosted gold deposits in Wutai Mountain area. Prog. Precambrian Res. 22, 11–17.
Ma, X.D., Guo, J.H., Liu, F., Qian, Q., Fan, H.R., 2013. Zircon U–Pb ages, trace elements and Nd–Hf isotopic geochemistry of Guyang sanukitoids and related rocks: implications for the Archean crustal evolution of the Yinshan block, North China Craton. Precambrian Res. 230, 61–78.
Manikyamba, C., Balaram, V., Naqvi, S.M., 1993. Geochemical signatures of polygenetic origin of a banded iron formation (BIF) of the Archaean Sandur greenstone belt (schist belt) Karnataka nucleus, India. Precambrian Res. 61, 137–164.
McLennan, S.M., 1989. Rare earth elements in sedimentary rocks: influence of provenance and sedimentary processes. In: Lipin, B.R., McKay, G.A. (Eds.), Geochemistry and Mineralogy of Rare Earth Elements, Rev. Miner. 21. , pp. 169–200 (Mineralogical Society of America).
McLennan, S.M., Hemming, S., McDaniel, D.K., Hanson, G.N., 1993. Geochemical approaches to sedimentation, provenance, and tectonics. In: Johnson, M.J., Basu, A. (Eds.), Processes Controlling the Composition of Clastic Sediments. GSA Special Paper 284. GSA, Boulder, CO.
Metcalf, R.V., Shervais, J.W., 2008. Suprasubduction-zone ophiolites: is there really an ophiolites conundrum. In: Wright, J.E., Shervais, J.W. (Eds.), Ophiolites Arcs, and Batholiths: A Tribute to Cliff Hopson. Geological Society of America Special Paper, vol. 938, pp. 191–222.
Mloszewska, A.M., Pecoits, E., Cates, N.L., Mojzsis, S.J., O'Neil, J., Robbins, L.J., Konhauser, K.O., 2012. The composition of Earth's oldest iron formations: the Nuvvuagittuq Supracrustal Belt (Québec, Canada). Earth Planet. Sci. Lett. 317, 331–342.
Niu, X.L., Li, J.H., 2006. Geochronology and Geological Event Sequences of Hengshan–Wutai Precambrian Complex. Acta Sci. Nat. Univ. Pekin. 1, 1–7.
Niu, X.L., Li, J.H., Feng, J., 2009. Origin of the Neoarchean massive sulphide deposits in Wutaishan Mt: an indication for the submarine exhalation from the microstructures. Adv. Earth Sci. 24, 1009–1014.
Parman, S.W., Grove, T.L., Dann, J.C., 2001. The production of Barberton komatiites in an Archean subduction zone. Geophys. Res. Lett. 28, 2513–2516.
Pearce, J.A., 1982. Trace element characteristics of lavas from destructive plate boundaries. In: Thorpe, R.S. (Ed.), Andesites. Wiley, Chichester, pp. 525–548.
Pearce, J.A., 2008. Geochemical fingerprinting of oceanic basalts with applications to ophiolite classification and the search for Archean oceanic crust. Lithos 100, 14–48.
Pearce, J.A., Peate, D.W., 1995. Tectonic implications of the composition of volcanic arc magmas. Annu. Rev. Earth Planet. Sci. Lett. 23, 251–285.
Pecoits, E., Gingras, M.K., Barley, M.E., Kappler, A., Posth, N.R., Konhauser, K.O., 2009. Petrography and geochemistry of the Dales Gorge banded iron formation: paragenetic sequence, source and implications for palaeo-ocean chemistry. Precambrian Res. 172, 163–187.
Planavsky, N., Bekker, A., Rouxel, O.J., Kamber, B.S., Hofmann, A.W., Knudsen, A., Lyons, T.W., 2010. Rare earth element and yttrium compositions of Archean and paleoproterozoic Fe formations revisited: new perspectives on the significance and mechanisms of deposition. Geochim. Cosmochim. Acta 74, 6387–6405.
Polat, A., Hofmann, A.W., Rosing, M.T., 2002. Boninite-like volcanic rocks in the 3.7–3.8 Ga Isua greenstone belt West Greenland: geochemical evidence for intra-oceanic subduction zone processes in the early Earth. Chem. Geol. 184, 231–254.
Polat, A., Kusky, T., Li, J.H., Fryer, B., Kerrich, R., Patrick, K., 2005. Geochemistry of Neoarchean (ca. 2.55–2.50 Ga) volcanic and ophiolitic rocks in the Wutaishan greenstone belt central orogenic belt, North China Craton: implications for geodynamic setting and continental growth. Geol. Soc. Am. Bull. 117, 1387–1399.
Puchtel, I., 2004. 3.0 Ga Olondo Greenstone belt in the Aldan Shield E. Siberia. In: Kusky, T. (Ed.), Precambrian Ophiolites and Related Rocks. Developments in Precambrian Geology. Elsevier, Amsterdam, pp. 405–423.
Rasmussen, B., Meier, D.B., Krapez, B., Muhling, J.R., 2013. Iron silicate microgranules as precursor sediments to 2.5-billion-year-old banded iron formations. Geology 41, 435–438.
Rolland, Y., Galoyan, G., Bosch, D., Sosson, M., Corsini, M., Fornari, M., Verati, C., 2009. Jurassic back-arc and Cretaceous hot-spot series In the Armenian ophiolites: implications for the obduction process. Lithos 112, 163–187.
Ross, M., Papike, J.J., Shaw, K.W., 1969. Exsolution textures in amphiboles as indicators of subsolidus thermal histories. Mineral. Soc. Am. Spec. Pap. 2, 275–299.
Rudnick, R.L., Gao, S., 2003. Composition of the continental crust. In: Rudnick, R.L. (Ed.), The Crust, vol. 3. In: Holland, H.D., Turekian, K.K. (Eds.), Treatise on Geochemistry, Elsevier-Pergamon, Oxford, pp. 1–64.
Rye, R., Holland, H.D., 2000. Geology and geochemistry of paleosols developed on the Hekpoort basalt, Pretoria Group, South Africa. Am. J. Sci. 300, 85–141.
Shen, Q.H., Song, H.X., Zhao, Z.R., 2009. Characteristics of rare earth elements and trace elements in Hanwang Neo-Archaean banded iron formations, Shandong province. Acta Geosci. Sin. 30, 693–699.
Shimizu, K., Nakamura, E., Maruyama, S., 2005. The geochemistry of ultramafic to mafic volcanics from the Belingwe Greenstone belt, Zimbabwe: magmatism in an Archean continental large igneous province. J. Petrol. 46, 2367–2394.
Shuto, K., Ishimoto, H., Hirahara, Y., Sato, M., Matsui, K., Fujibayashi, N., Takazawa, E., Yabuki, K., Sekine, M., Kato, M., Rezanov, A.I., 2006. Geochemical secular variation of magma source during early to middle Miocene time in the Niigata area, NE Japan: asthenosphere mantle upwelling during back-arc basin opening. Lithos 86, 1–33.
Spear, F., 1993. Metamorphic Phase Equilibria and Pressure–Temperature–Time Paths. Mineralogical Society of America, Washington, DC, pp. 799.
Srivastava, R.K., Singh, R.K., Verma, S.P., 2004. Neoarchaean mafic volcanic rocks from the southern Bastar greenstone belt, Central India: petrological and tectonic significance. Precambrian Res. 131, 305–322.
Stacey, J.S., Kramers, J.D., 1975. Approximation of terrestrial lead isotope evolution by a two-stage model. Earth Planet. Sci. Lett. 26, 207–221.
Sun, S.S., McDonough, W.F., 1989. Chemical and isotopic systematics of oceanic basalts: implications for mantle composition and processes. Geol. Soc. Lond. Spec. Publ. 42, 313–345.
Thurston, P.C., Kamber, B.S., Whitehouse, M., 2012. Archean cherts in banded iron formation: insight into Neoarchean ocean chemistry and depositional processes. Precambrian Res. 214, 227–257.

Tian, Y.Q., 1991. Geology and Mineralization of the Wutai–Hengshan Greenstone Belt. Shanxi Science and Technology Press, Taiyuan, China, 270 pp.
Trendall, A.F., 2002. The significance of iron-formation in the Precambrian stratigraphic record. Spec. Publ. Int. Assoc. Sedimentol. 33, 33–66.
Trendall, A.F., Morris, R.C., 1983. Iron Formations: Facts and Problems. Elsevier Scientific Publishers Inc., Amsterdam.
Wan, Y.S., Miao, P.S., Liu, D.Y., Yang, C.H., Wang, W., Wang, H.C., Wang, Z.J., Dong, C.Y., Du, L.L., Zhou, H.Y., 2010. Formation ages and source regions of the Palaeoproterozoic Gaofan Hutuo and Dongjiao Groups in the Wutai and Dongjiao areas of the North China Craton from SHRIMP U–Pb dating of detrital zircons: Resolution of debates over their stratigraphic relationships. Chin. Sci. Bull. 55, 1278–1284.
Wan, Y.S., Dong, C.Y., Xie, H.Q., Wang, S.J., Song, M.C., Xu, Z.Y., Wang, S.Y., Zhou, H.Y., Ma, M.Z., Liu, D.Y., 2012a. Formation ages of early Precambrian BIFs in the North China Craton: SHRIMP zircon U–Pb dating. Acta Geol. Sin. 86, 1447–1478.
Wan, Y.S., Wang, S.J., Liu, D.Y., Wang, W., Kröner, A., Dong, C.Y., Yang, E.X., Zhou, H.Y., Xie, H.Q., Ma, M.Z., 2012b. Redefinition of depositional ages of Neoarchean supracrustal rocks in western Shandong Province, China: SHRIMP U–Pb zircon dating. Gondwana Res. 21, 768–784.
Wang, C.L., Zhang, L.C., Lan, C.Y., Dai, Y.P., 2014. Rare earth element and yttrium compositions of the Paleoproterozoic Yuanjiacun BIF in the Lüliang area and their implications for the great oxidation event (GOE). Sci. China Earth Sci.
Wang, W., Zhai, M.G., Wang, S.J., Santosh, M., Du, L.L., Xie, H.Q., Lv, B., Wan, Y.S., 2013. Crustal reworking in the North China Craton at ~2.5 Ga: evidence from zircon U–Pb age Hf isotope and whole rock geochemistry of the felsic volcano-sedimentary rocks from the western Shandong Province. Geol. J. 48, 406–428.
Wang, Z.H., Wilde, S.A., Wang, K.Y., Yu, L.J., 2004. A MORB-arc basalt–adakite association in the 2.5 Ga Wutai greenstone belt: Neoarchaean magmatism and crustal growth in the North China Craton. Precambrian Res. 131, 323–343.
Wilde, S.A., Cawood, P.A., Wang, K.Y., 1997. The relationship and timing of granitoid evolution with respect to felsic volcanism in the Wutai complex, North China Craton. In: Proceedings of the 30th IGC, Precambrian Geology & Metamorphic Petrology 17, pp. 75–88.
Wilde, S.A., Cawood, P.A., Wang, K.Y., Nemchin, A., Zhao, G.C., 2004. Determining Precambrian crustal evolution in China: a case-study from Wutaishan Shanxi province, demonstrating the application of precise SHRIMPU–Pb geochronology. In: Malpas, J., Fletcher, C.J.N., Ali, J.R., Aichison, J.C. (Eds.), Aspects of the Tectonic Evolution of China: Geological Society of London, Special Publication 226. , pp. 5–26.
Wilde, S.A., Cawood, P.A., Wang, K.Y., Nemchin, A.A., 2005. Granitoid evolution in the late Archean Wutai complex: North China Craton. J. Asian Earth Sci. 24, 597–613.
Winchester, J.A., Floyd, P.A., 1977. Geochemical discrimination of different magma series and their differentiation products using immobile elements. Chem. Geol. 20, 325–343.
Windley, B.F., 1995. The Evolving Continents, third ed. John Wiley & Sons, Chichester, England, pp. 377–385 (pp. 447–462).
Wyman, D., Kerrich, R., 2012. Geochemical and isotopic characteristics of Youanmi terrane volcanism: the role of mantle plumes and subduction tectonics in the western Yilgarn Craton. Aust. J. Earth Sci. 59, 1–24.
Zhai, M.G., Santosh, M., 2013. Metallogeny of the North China Craton: link with secular changes in the evolving earth. Gondwana Res. 24, 275–297.
Zhai, M.G., Windley, B.F., 1990. The Archean and early Proterozoic iron formation of North China: their characteristics, geotectonic relations, chemistry and implications for crustal growth. Precambrian Res. 48, 267–286.
Zhang, L.C., Zhai, M.G., Zhang, X.J., Xiang, P., Dai, Y.P., Wang, C.L., Pirajno, F., 2012a. Formation age and tectonic setting of the Shirengou Neoarchean banded iron deposit in eastern Hebei province: constraints from geochemistry and SIMS zircon U–Pb dating. Precambrian Res. 222, 325–338.
Zhang, L.C., Zhai, M.G., Wan, Y.S., Guo, J.H., Dai, Y.P., Wang, C.L., Liu, L., 2012b. Study of the Precambrian BIF-iron deposits in the North China Craton: progresses and questions. Acta Petrol. Sin. 28, 3431–3445.
Zhang, X.J., Zhang, L.C., Xiang, P., Wan, B., Pirajno, F., 2011. Zircon U–Pb age, Hf isotopes and geochemistry of Shuichang Algoma-type banded iron-formation, North China Craton: constraints on the ore-forming age and tectonic setting. Gondwana Res. 20, 137–148.
Zhang, Y.Z., Wang, Y.J., Geng, H.Y., Zhang, Y.H., Fan, W.M., Zhong, H., 2013. Early Neoproterozoic (~850 Ma) back-arc basin in the Central Jiangnan Orogen (Eastern South China): geochronological and petrogenetic constraints from meta-basalts. Precambrian Res. 231, 325–342.
Zhao, G.C., Cawood, P.A., Lu, L.Z., 1999. Petrology and P–T history of the Wutai amphibolites: implications for tectonic evolution of the Wutai Complex China. Precambrian Res. 93, 181–199.
Zhao, G.C., Wilde, S.A., Cawood, P.A., Sun, M., 2001. Archean blocks and their boundaries in the North China Craton: lithological, geochemical, structural and P-T path constraints and tectonic evolution. Precambrian Res. 107, 45–73.
Zhao, G.C., Wilde, S.A., Cawood, P.A., Sun, M., 2002. SHRIMP U–Pb zircon ages of the Fuping complex: implications for Late Archean to Paleoproterozoic accretion and assembly of the North China Craton. Am. J. Sci. 302, 191–226.
Zhao, G.C., Sun, M., Wilde, S.A., Li, S.Z., 2005. Late Archean to Paleoproterozoic evolution of the North China Craton: key issues revisited. Precambrian Res. 136, 177–202.
Zhao, G.C., Kröner, A., Wilde, S.A., Sun, M., Li, S.Z., Li, X.P., Zhang, J., Xia, X.P., He, Y.H., 2007. Lithotectonic elements and geological events in the Hengshan–Wutai-Fuping belt: a synthesis and implications for the evolution of the Trans-North China Orogen. Geol. Mag. 144, 753–775.
Zhang, Y., Gu, X.X., Li, Y.H., Dong, S.Y., Cheng, W.B., 2010. Element geochemical characteristics of the Wangjiazhuang banded magnetite-quartzite deposit in Yuanping City, Shanxi Province, and its geological significance. Geoscience 24, 69–79.
Zhao, R.F., 2012. Petrogenesis of late Archean TTG gneisses and Paleoproterozoic potassic granites in Hengshan terrane, North China Craton. Doctoral dissertation. University of Chinese Academy of Sciences, 143 pp.